Chapter 5

Prototyping a Gas Sensors Using CeO_2 as a Matrix or Dopant in Oxide Semiconductor Systems

Lucian Pîslaru-Dănescu, Gabriela Telipan, Ioana Ion and Virgil Marinescu

Additional information is available at the end of the chapter

http://dx.doi.org/10.5772/intechopen.80801

Abstract

In this chapter, two important aspects of using CeO_2 in the field of gas sensors are presented. Firstly, for CO_2 detection in the range of 0–5000 ppm, a binary semiconductor oxides CeO_2-Y_2O_3 was used. Secondly, as a dopants, in oxide semiconductor systems, used to detect the NO_2. In this case, CeO_2 is used as a dopant in hybride composite, consisting of reduced graphene oxide/ZnO, in order to increase the sensibility in NO_2 detection at low concentration in the range of 0–10 ppm. The structural and morphological characterization of sensitive materials by X-ray diffraction, SEM, adsorption desorption isotherms, thermal analysis and RAMAN spectroscopy are presented. Also, the sensing element of the sensor that detects the NO_2 is achieved by depositing the nanocomposite material on the interdigital grid. The electronic conditioning signal from the sensing element is achieved by using a Wheatstone bridge together with an instrumentation operational amplifier.

Keywords: ceria oxide, yttrium oxide, zinc oxide, reduced graphene oxide, sensing element, electronic conditioning, X-ray diffraction, scanning electron microscopy

1. Introduction

Cerium represents one of the most abundant elements in the Earth's crust (66.5 ppm) than copper (60 ppm) or tin (2.3 ppm). Ce possesses an unique electronic configuration ([Xe] $4f^2 6s^2$), and presents two common valence states Ce^{3+} and Ce^{4+} [1–3], which give CeO_2 excellent chemical and physical properties: 1/4 O_2, at most, can be released from each CeO_2 unit cell. It serves as an active oxygen donor in many reactions, such as three-way catalytic reactions to eliminate toxic

automobile exhaust [1, 4], the low-temperature water gas shift reaction [1, 5], oxygen sensors, oxygen permeation membrane systems and fuel cells [1, 6]. Cerium oxide CeO_2 is a semiconductor oxide with a band gap energy (3.19 eV) [7, 8]. The crystalline structure consists of a cubic fluorite structure (Fm3m) with a cell parameter of 5.41 Å at room temperature and presents a high dielectric constant ε = 26, almost of silicon, that it makes use in spintronic devices with silicon microelectronic devices [9, 10]. Synthesis of CeO_2 nanoparticles comprise various methods as: solvothermal [2, 11, 12], sol gel [2, 13, 14], sonochemical [2, 15], hydrolysis [2, 16], hydrothermal [2, 17, 18], precipitation [2, 19] and reverse micelles [2, 20]. The dual oxidation state mentioned above means that these nanoparticles have oxygen vacancies or defects [19]. The loss of oxygen and the reduction of Ce^{4+} to Ce^{3+} in accord with Eq. 1, is accompanied by creation of an oxygen vacancy. This property is responsible for the interesting redox chemistry exhibited by ceria nanoparticles and makes them attractive for many catalytic applications [21].

$$CeO_2 \underset{oxidizing}{\overset{reducing}{\longleftrightarrow}} CeO_{2-y} + {}^{y}/_{2}O_2 \tag{1}$$

Also all ceria applications are based on its potential redox between Ce^{3+} and Ce^{4+}, high oxygen affinity and absorption/excitation energy bands associated with the electronic structure [22]. Another important property of CeO_2 consists in their ability to release and absorb oxygen during alternating redox conditions and hence to function as oxygen buffer. The addition of dopants leads to increase of concentration of oxygen vacancies and improves the thermal stability of the parent oxide [23]. Also, CeO_2 presents a great chemical stability and high diffusion coefficient with values between 10^{-8} and 10^{-6} cm^2/s in the temperature range of 800–2200 K coming from oxygen vacancies ($V_o^{\cdot}$ has been used for gas sensing for oxygen, NO_x, acetone and H_2S sensors). Besides, CeO_2 is also used for improving sensing properties of semiconductor oxides such as ZnO, TiO_2 and In_2O_3 [24, 25]. On the other hand, the ionic conductivity of CeO_2 is improved by doping with rare earth oxides such as Sm_2O_3, Gd_2O_3 and Y_2O_3 and the size of conductivity of the doped ceria depends on the ionic radius of the doping ion. The introduction of trivalent ions in ceria leads to production of anion vacancies

Sensitive material	Gas detected	Range concentration, [ppm]/[%]	Operation temperature, [°C]	Detection limit, [ppm]	Response/ recovery time, [s]	Ref.
CeO_2-SnO_2	CO	0–500 ppm	430	<5	26/30	[27]
ZnO/Al_2O_3/CeO_2	ethanol	0–2000 ppm	260	*	2/10	[28]
CeO_2-Fe_2O_3	methanol	1–1000 ppm	400	1–3	*	[29]
CeO_2	formaldehyde	0.5–50 ppm	30	—	36/1	[30]
CeO_2 activated ZnO-TiO_2	CO_2	286 ppm exposure	290	*	24/72	[31]
$Ce_{(1-x)}$ Zr_xO_2	O_2	1–100%	500–700	*	*	[32]

*Data unavailable.

Table 1. Gas detection with sensitive materials based on CeO_2.

http://dx.doi.org/10.5772/intechopen.80801

which may enhance catalytic and gas sensing properties [26]. In **Table 1,** several sensitive materials based on ceria for gas detection and their gas sensing characteristics is presented.

As doping with other ions could lead to enhanced activity for different reasons. Ceria doped with pentavalent ions as Nb, could insert extra oxygen anions that would be more easily removed [26]. In this chapter, the mixed oxides CeO_2-Nb_2O_5, Y_2O_3-doped CeO_2 as sensitive materials for CO_2 detection and sensitive materials composed from CeO_2-doped rGO (reduced graphene oxide) and CeO_2-doped rGO-ZnO for NO_2 detection are presented.

To conditioning the signal provided by sensing element, high-performance electronic circuits such as precision operational amplifiers, digital analogue converters and analog multipliers have been used [33, 34].

2. Sensor for CO_2 detection with mixed binary oxide CeO_2-Nb_2O_5 sensitive material

Niobium oxide has some properties that make it in principal as promising for catalytic applications. Niobia-based materials are effective catalysts in selective oxidation reactions due to its redox properties. Also, niobia-doped ceria materials have shown a good carbon deposition and excellent properties as solid oxide fuel cell (SOFC) anodes [35]. Nb^{5+} ions (ionic radius of Nb^{5+}: 78 pm) may initiate the reduction of Ce^{4+} to Ce^{3+} by the doping Nb into the CeO_2 structure, which results in formation of oxygen vacancies. Using the Kröger-Vink notation, it can mention two mechanisms for the dissolution: one of which occurs by electronic compensation (Eq. 2) and the other by consumption of vacancies (Eq. 3), as shown below [3, 36, 37].

$$Nb_2O_5 + Ce_M{}^{*} \rightarrow 2Nb_M^{\cdot} + 4O_0^{*} + \frac{1}{2}O_2 + 2Ce_M^{/} \tag{2}$$

$$Nb_2O_5 + V_0^{\cdot\cdot} \rightarrow 2Nb_M^{\cdot} + 5O_o^{*} \tag{3}$$

where O_o^{*}, $V_o^{\cdot\cdot}$ represent oxygen and oxygen vacancies on the oxygen sites, Ce_M^{*}, $Ce_M^{/}$ represent cerium (Ce^{4+}) and negatively charged cerium ions (Ce^{3+}) on metal sites M, $Nb_M^{\cdot}$ metal vacancy. Nb_2O_5 it is known as an n-type oxide semiconductor with a band gap about 3.4 eV. Because of its good physicochemical properties and structural isotropy, it is used in other range of applications such as: in construction of gas sensing, field-emission displays and microelectronics electrochromics display and photoelectrodes [38].

2.1. Synthesis of mixed oxides CeO_2-Nb_2O_5 sensitive material

In our case, we used the mixed binary oxides CeO_2-Nb_2O_5 for CO_2 detection. Sensitive element is composed from mechanical mixing of CeO_2 (97%) and Nb_2O_5 (3%); both reagents purchased from Merck. The powder oxides were treated with a few drops of ethylic alcohol for ink obtaining and then introduced in a ball mill for homogenization followed by calcination at 500, 600 and 800°C for 1 hour. The powder calcined at 600°C was pressed in disc form at 2 tons force/cm^2 with the dimensions ∅4 × 1 mm and mounted on the ambasis transistor. The sensor image is showed in **Figure 1** [39].

Figure 1. Image of the CO_2 sensor made with mixed oxides CeO_2-Nb_2O_5 sensitive material.

2.2. Structural characterization

Calcined mixed powder oxides were characterized by X-ray diffraction using a diffractometer-type X Bruker-AXS type D8 ADVANCE in conditions: CuK_α radiation (λ =1.54059 Å), 40 kV/40 mA, filter k_β of Ni. pas: 0.04°, measuring time on point: 1 s, measure range 2θ = 10–100°. The mixed oxides powder with composition CeO_2–3%Nb_2O_5 was calcined at 500, 600 and 800°C for 1 hour. It shows a cubic phase for CeO_2 and orthorhombic phase for Nb_2O_5, **Figure 2**. Also, for this powder that was calcined at 800°C, was identified in addition a hexagonal Ce_2O_3 phase (**Figure 3**). It obtain for CeO_2 cell parameter a = b = c = 5.407 Å. This is in accord with

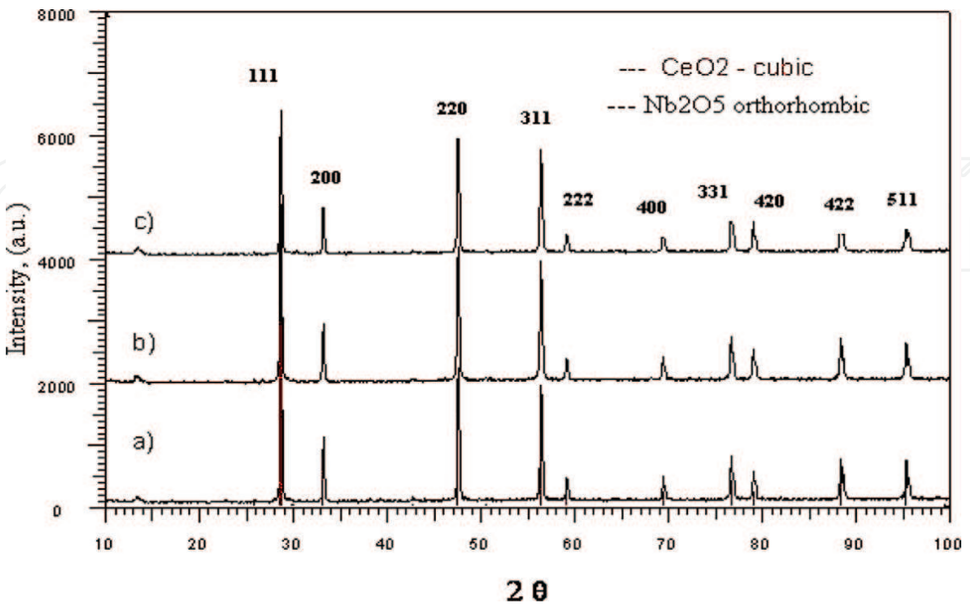

Figure 2. X-ray diffraction of CeO_2-Nb_2O_5 calcinated at: (a) 500°C; (b) 600°C and (c) 800°C.

http://dx.doi.org/10.5772/intechopen.80801

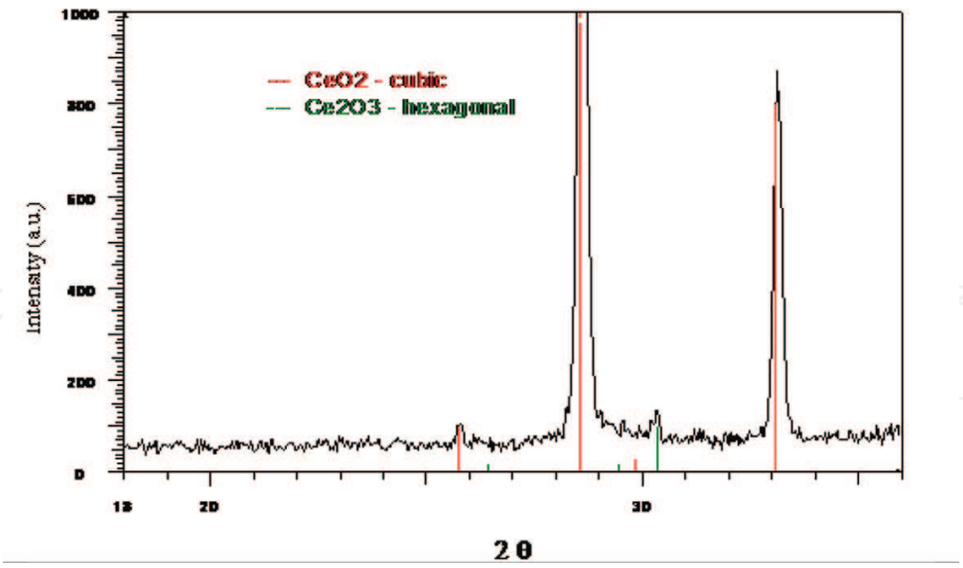

Figure 3. X-ray diffraction of CeO_2-Nb_2O_5 calcinated at 800°C.

theoretical value of a = 5.404 Å as well as in according with card number 03–065-5923. The cell parameters for Nb_2O_5 orthorhombic phase were a = 6.175 Å, b = 29.175 Å and c = 3.930 Å in accord with card number 30-0873 [4]. Corresponding to hkl (Miller indices) 111, 200, 220 and 311, the crystallites size determined with Scherrer formula give values of 160.9, 145.6, 117.4 and 63.5 nm.

2.3. CO_2 gas sensor made with mixed oxides CeO_2-Nb_2O_5 sensitive material tested in automated process mode

The gas sensors testing were performed with the apparatus as presented in **Figure 4.** It is realized by SYSCOM-18 Romania for National Institute for Research and Development in

Figure 4. The testing gas sensor installation.

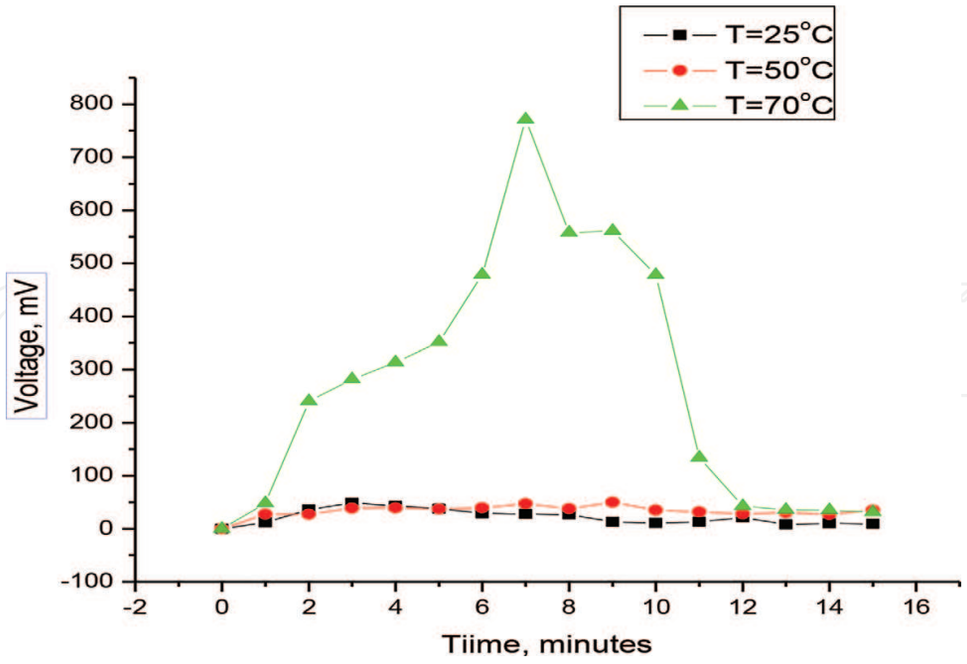

Figure 5. Variation of the voltage depending on time for CO_2 sensor, made with mixed oxides CeO_2-Nb_2O_5 sensitive material.

Electrical Engineering ICPE-CA. The voltage measurements were effected by testing module, in automated process mode. A control panel provides a lot of measuring values, at rate 1/10 s. The bench of testing for the gas sensor consists in an enclosure where there are set of testing conditions for the sensor as well as in connected equipment. The whole process of testing is automated, being controlled by a programmable automaton. The gas for testing is introduced in a controlled way in the testing enclosure, through a mass debit meter. In the testing, enclosure is set a constant temperature, controlled by a temperature regulator.

The gas testing was done in concentration of 10,000 ppm CO_2 at the 25, 50 and 70°C chamber test temperature. The sensor was developed the voltages values of 48, 50 and 770 mV (**Figure 5**) [39].

The experimental data shows a good sensor response for CO_2 detection with increasing temperature.

2.4. Signal conditioning of the sensing element for CO_2 detection with mixed binary oxide CeO_2-Nb_2O_5 sensitive material

The Analog Devices AD620 operational amplifier is used to build the signal conditioning electronic module, provided by the sensing element. A preamp section comprised of Q1 and Q2, **Figure 6**, provides additional gain up front. Feedback through the Q1-A1-R1 loop and the Q2-A2-R2 loop maintains a constant collector current through the input devices Q1 and Q2, thereby impressing the input voltage across the external gain setting resistor, R_G.

This creates a differential gain from the inputs to the A1/A2 outputs given by Eq. (4):

http://dx.doi.org/10.5772/intechopen.80801

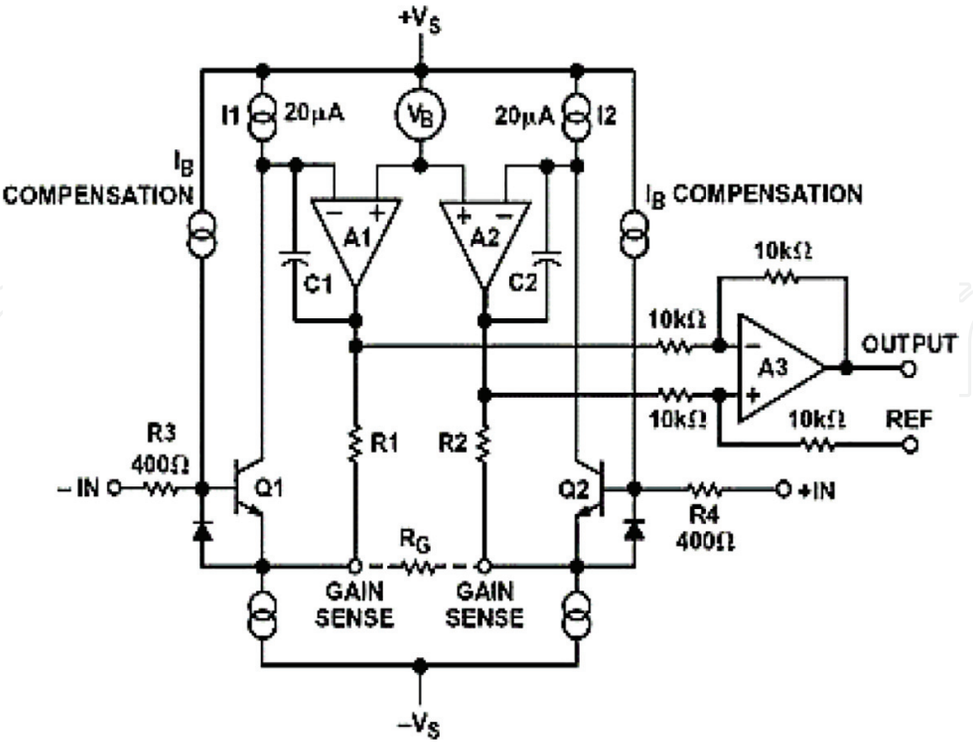

Figure 6. A simplified schematic of the AD620 [39].

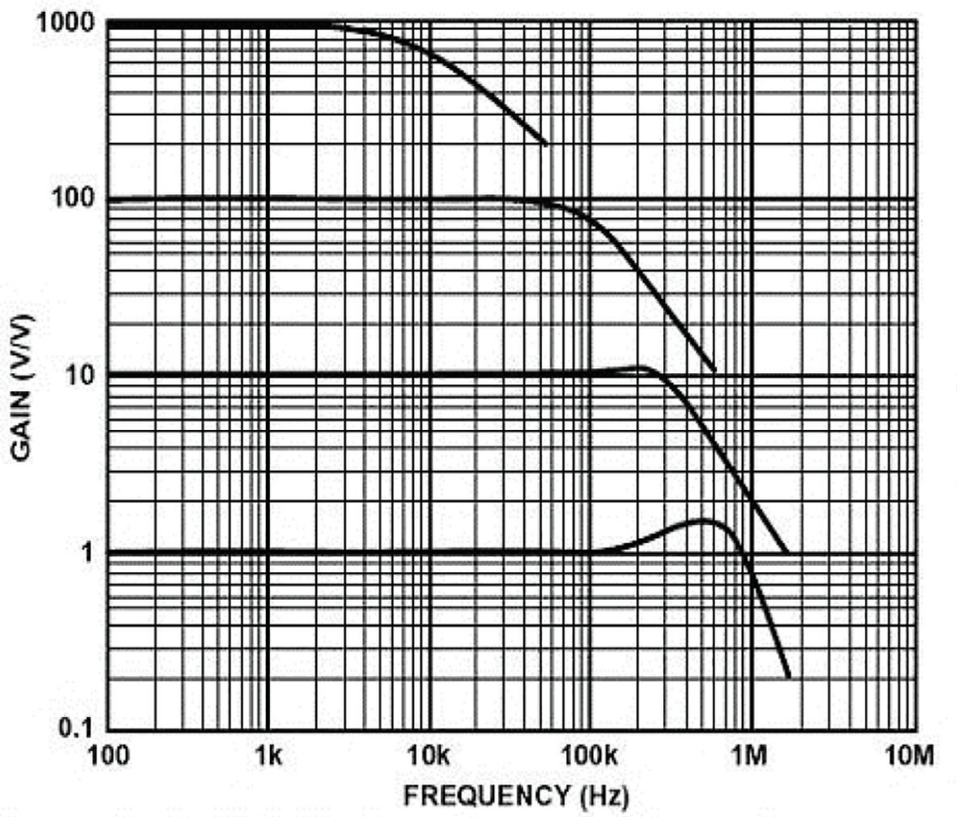

Figure 7. AD620 closed-loop gain versus frequency [39].

$$G = \frac{R1 + R2}{R_G} + 1 \tag{4}$$

The unity-gain subtractor, A3, removes any common-mode signal, yielding a single-ended output referred to the REF pin potential. The value of R_G also determines the transconductance of the preamp stage [34]. As R_G is reduced for larger gains, the transconductance increases asymptotically to that of the input transistors. The open-loop gain is boosted for increasing programmed gain, thus reducing gain related errors. Also, the gain bandwidth product (determined by C1, C2 and the preamplifier transconductance, **Figure 6**) increases with programmed gain, thus optimizing the amplifier's frequency response. In **Figure 7**, the closed-loop gain of AD620 versus frequency is shown. Finally, the input voltage noise is reduced to 9 nV/√*Hz*, which is determined mainly by the collector current and base resistance of the input devices. The internal gain resistors, R1 and R2, are laser trimmed to an absolute value of 24.7 kΩ, allowing the gain to be programmed accurately with a single external resistor. The gain equation is Eq. (5).

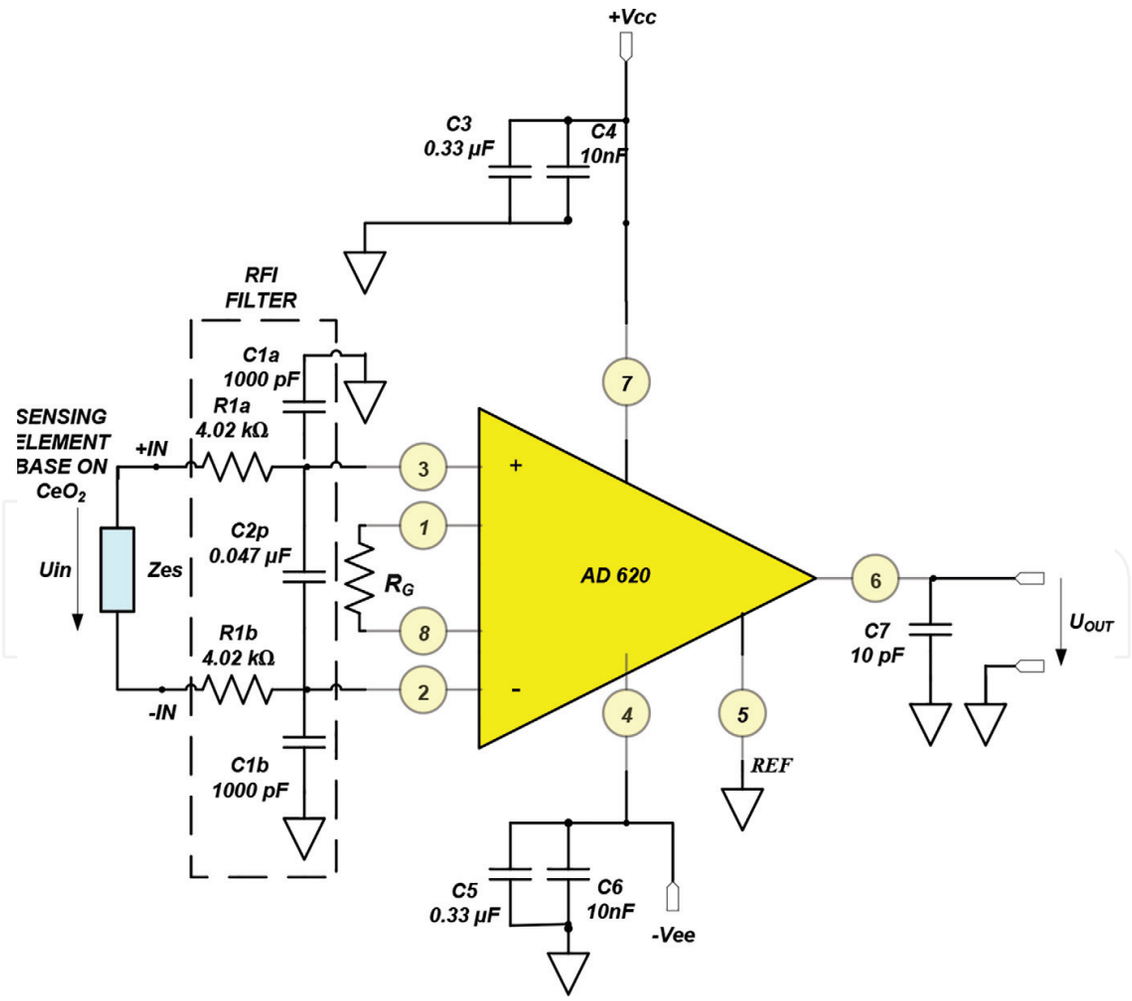

Figure 8. The electronic module for signal conditioning provided by sensing element, designing with AD620 analog devices.

http://dx.doi.org/10.5772/intechopen.80801

$$G = \frac{49.4k\Omega}{R_G} + 1 \tag{5}$$

So that,

$$R_G = \frac{49.4k\Omega}{G - 1} \tag{6}$$

where the resistor R_G in kΩ, according to Eq. (6).

The value of 24.7 kΩ was chosen so that standard 1% resistor values could be used to set the most popular gains. For the input resistors, R_{1a} and R_{1b} were used, capacitor C2p approximately five times to 0.047 μF to provide adequate RF attenuation (**Figure 8**). With the values shown, the circuit −3 dB bandwidth is approximately 400 Hz and noise levels 12 nV/√*Hz*. It requires the circuitry preceding the in-amp to drive a lower impedance load and results in somewhat less input overload protection. The output signal V_{OUT} (**Figure 8**) is a common mode voltage, picked at the output of the operational amplifier. The capacitor groups, 0.01 μF and 0.33 μF make a decoupling of the supply voltage (**Figure 8**) in the immediate closeness of the operational amplifiers. The supply voltage $+V_{cc}$ and $-V_{ee}$, respectively, stabilized is differentiated, $\pm 15V_{cc}$, in comparison with the reference potential bar.

3. Sensor for CO_2 detection with Y_2O_3-doped CeO_2 sensitive material

The ion conductivity of CeO_2 can be significantly improved upon substitution with some trivalent oxides of lanthanides like Y_2O_3, Sm_2O_3 and Gd_2O_3, because the number of oxygen vacancy will be considerably increased for charge compensation. The electrical conductivity in doped ceria is influenced by factors such as: the dopant ion, the dopant concentration, the oxygen vacancy concentration and the defect association enthalpy. An example is constituted by combination Y_2O_3-doped CeO_2 which has been used usually as the solid electrolyte for moderate temperature solid oxide fuel cells [40]. In our case, we used the Y_2O_3-doped CeO_2 as sensitive material for CO_2 detection. For Y_2O_3-CeO_2 synthesis, it utilizes several methods such as hydrothermal [41], electrospinning [23], thermolysis [42] and sol gel [43].

3.1. Synthesis method

Sol gel method applied for synthesis of Y_2O_3-doped CeO_2 sensitive material, is in accord with ref. [44] and used as starting reagents $Ce(SO_4)_2 \times 4H_2O$ (97% purity, Merck) and $Y(NO_3)_3 \times 3H_2O$ (98% purity Karlsrushe GmbH in molar ratio CeO_2/Y_2O_3 = 4:1). The salts were dissolved in deionized water. To 100 ml salt solution, 25 ml solution of 1 M citric acid as chelating agent was added. To obtain gel, the salt solution was heated to 70°C under constant stirring. To this solution, 40 ml ethylene glycol was added to promote citrate polymerization and heated at 90°C. The gel formed was filtered, washed and heat treated in oven at 100°C. The powder obtained was calcined at 800°C for 2 hours. The powder was pressed to disc form using 10 ton force/cm^2, with dimensions diameter 4 mm, height 1 mm and then sinterized at 1100°C for 6 hours [44].

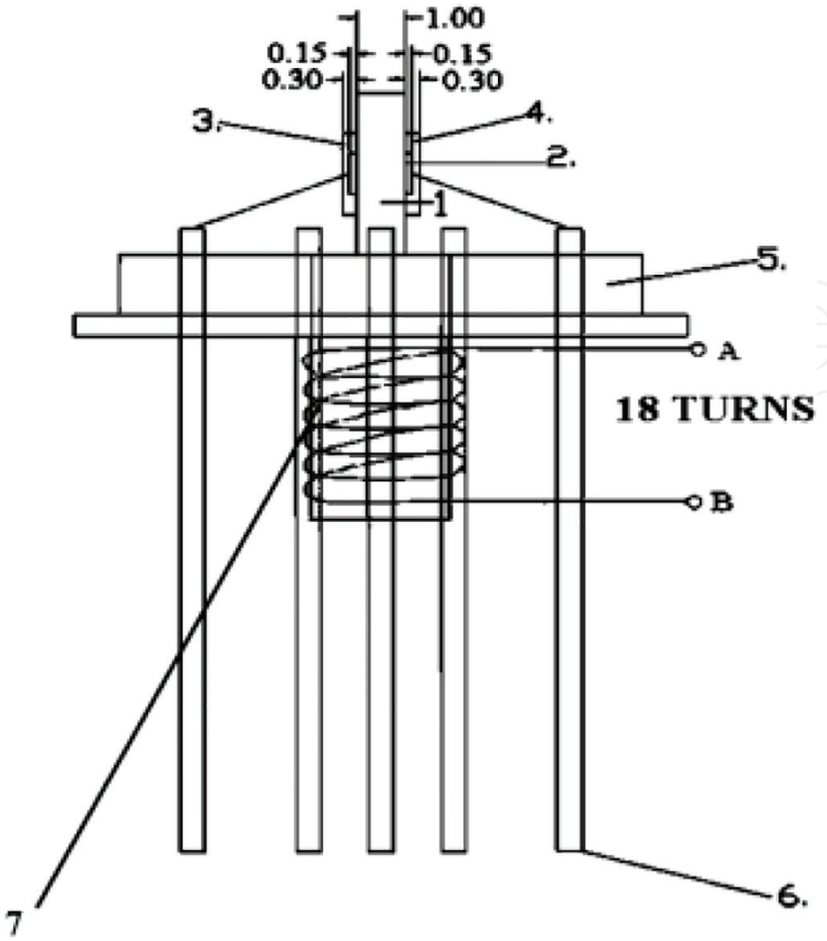

Figure 9. CO_2 sensor, component parts: 1. Ce_2O_2-Y_2O_3 disc; 2. Gold electrode, thin film deposition of Au, in the form of the disc; 3. Ag micro-wire connections; 4. The positioning piece; 5. TO-8 package plated base; 6. The pins; 7. A, B terminals of 18 turns heating resistance.

3.2. The construction of the sensor for CO_2 detection designed with Y_2O_3-doped CeO_2 sensitive material

On both sides of disc, gold electrodes in circular form with diameter of 1 mm was deposed. The gold was deposed by e-beam evaporation method using Baltzer equipment with conditions: pressure P = 10^{-5} Torr and current I = 8 mA, for 60 s time deposition. The disc with electrodes deposed was mounted on a 12 pin TO-8 package base. Below the base, the heater element composed of Ni wire with a diameter of 0.1 mm was placed, the winding is composed from 18 turns with a diameter of d = 3 mm. **Figure 9** shows how it built the CO_2 sensor [44].

3.3. Structural and morphological characterization of sensitive material Y_2O_3-doped CeO_2

Thermal analysis was performed with NETZSCH STA 409 simultaneous thermogravimetric balance, in the analysis conditions: inert atmosphere of argon, heating rate of 10°C/min in alumina crucible and the mass sample was 15.7 mg. **Figure 10** presents the thermal analysis TG, DTA and differential thermogravimetry (DTG) curves for the dried gel. The DTA curve

http://dx.doi.org/10.5772/intechopen.80801

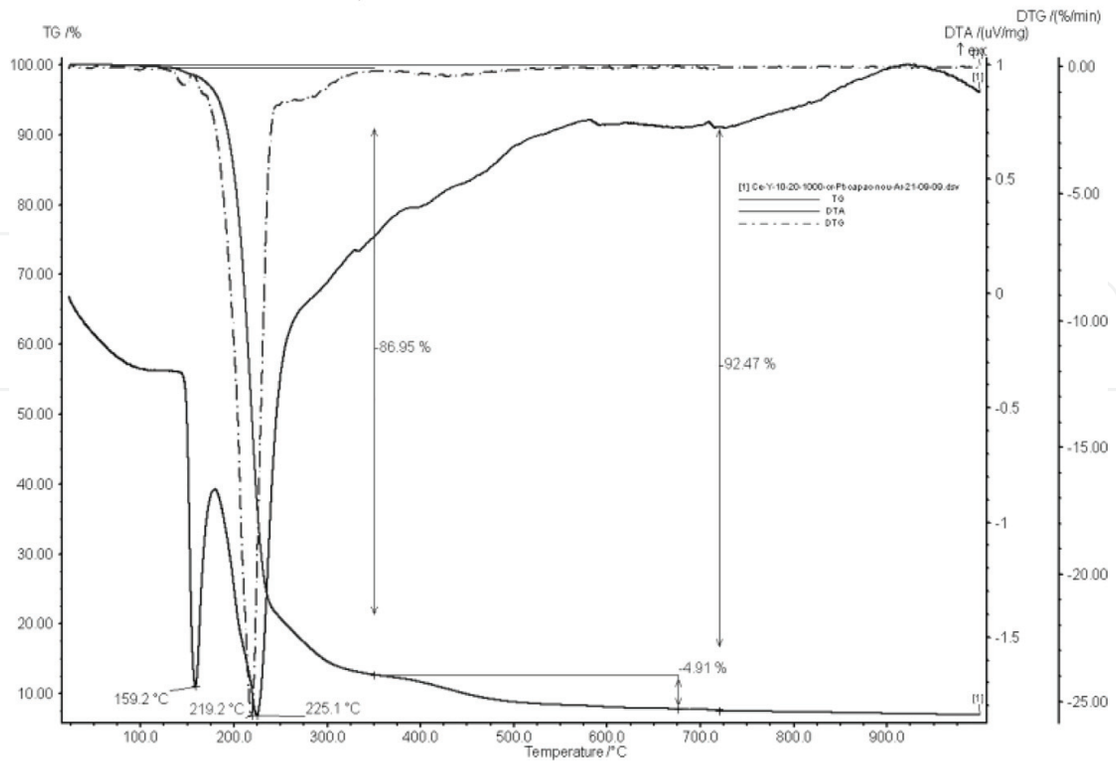

Figure 10. Thermal analysis TG, DTA and DTG curves for dried gel of CeO_2-Y_2O_3.

releases two endothermic peaks at 159.2 and 225.1°C. The last one has a correspondent in DTG curve at 219°C, the total mass loss was 86.95% from initial mass. Other thermal transformation appears at 430°C which represents on in a TG curve a loss of 4.91% which correspond to the decomposition of precursors, consisting in cerium sulfate and yttrium nitrate and in the end only Ce-Y-related oxides are obtained [44].

The X-ray diffraction patterns of the CeO_2-Y_2O_3 oxides powder calcinations at 800°C for 2 hours are shown in **Figure 11**. For comparison, **Figure 12** shows the X-ray diffraction for commercial CeO_2 powder. For this oxides system, the XRD pattern reveals the formation of well crystallized phases, CeO_2 indexed with the cubic fluorite structure and Y_2O_3 with cubic structure. Also, a secondary phase with cubic structure and composition $Ce_{0.6}Y_{0.4}O_{1.8}$ was identified [44].

Table 2 presents X-ray parameters for Y_2O_3-doped CeO_2, cell parameters and crystallite sizes determined with Scherrer formula.

The morphological structure of Y_2O_3-doped CeO_2 was investigate by SEM measurements using FESEM-FIB type Auriger model Carl Zeiss SMT GmbH at a high voltage acceleration of 2 and 3 kV. The SEM sample morphology was investigated trough SESI (combined detector in SEM chamber–Evernhart Thornley type with Faraday cup). **Figure 13** shows the SEM image for disc CeO_2-Y_2O_3 sintered, where it can be seen as a relative homogeneous structure and the crystallite sizes of CeO_2 and Y_2O_3 were in range of 26–54 nm in good accord with X-ray diffraction analysis. **Figure 14** shows the SEM images for CeO_2-Y_2O_3 powder calcined at

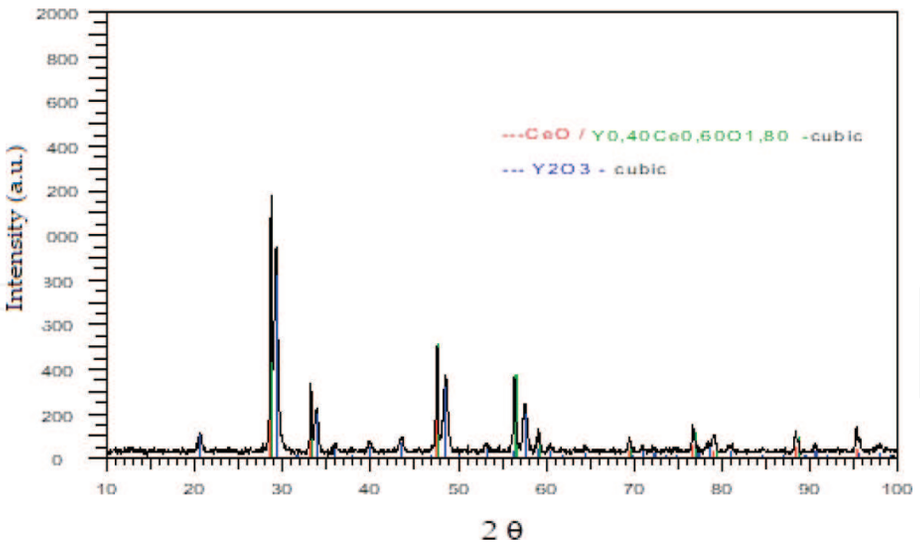

Figure 11. X-ray diffraction of Y_2O_3-doped CeO_2 synthesized by sol gel method.

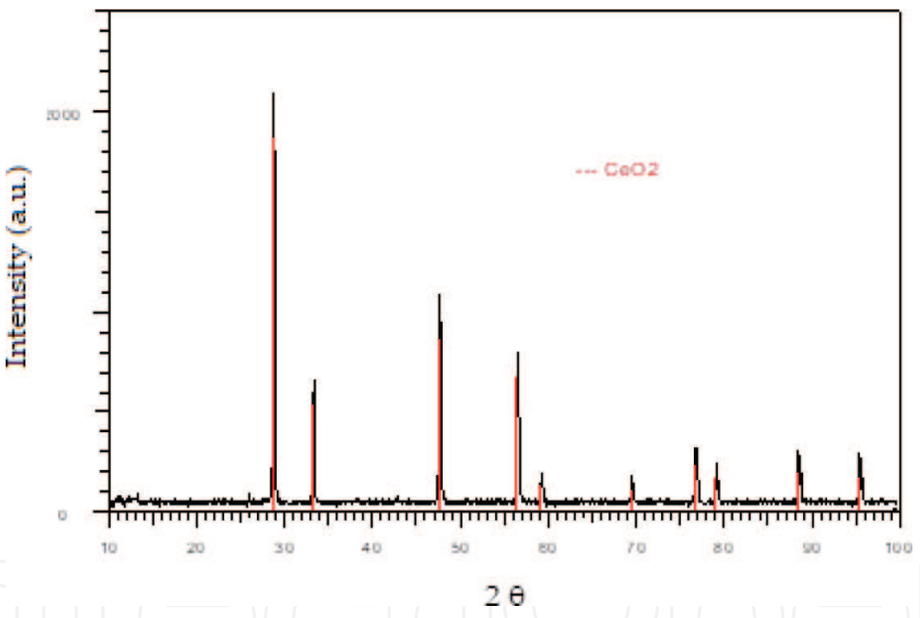

Figure 12. X-ray diffraction for commercial CeO_2.

800°C for 2 hours, where it can be see a nonhomogeneous structure composed by agglomerates [44].

N_2 adsorption desorption isotherms were performed with the AUTOSORB-1, Quantachrome Instruments, United Kingdom in the following conditions: working gas N_2, measured temperature: −196°C and relative pressure range P/Po = 0.001–0.99. For binary oxides CeO_2-Y_2O_3, powder calcined at 800°C for 2 hours, BET analysis revealed the results: the specific surface area was 3.13 m^2/g, the total volume of the pores was $1.066x10^{-3}$ cm^3/g and pore sizes of 8.93 Å. There is a specific ratio P/P_o = 0.02898 for the pores with diameters smaller than 6.9 Å [44].

Phase	Crystal structure	Unit cell parameter (Å) a = b = c		2Θ	Crystalline face indexes hkl	Crystallites-size (nm)
		Experimental	Theoretic card no.:			
CeO_2	Cubic	5.41325	5.41100 PDF 01-071-4199	28.536	111	48.1
Y_2O_3	Cubic	10.61131	10.61060 PDF 01-076-8044	29.121	222	27.0
$Y_{0.4}Ce_{0.6}O_{1.8}$	Cubic	5.39449	5.39300 PDF 01-075-0177	28.639	111	49.2
CeO_2 Merck	Cubic	5.384			111	154.9

Table 2. X-ray parameters for Y_2O_3-doped CeO_2.

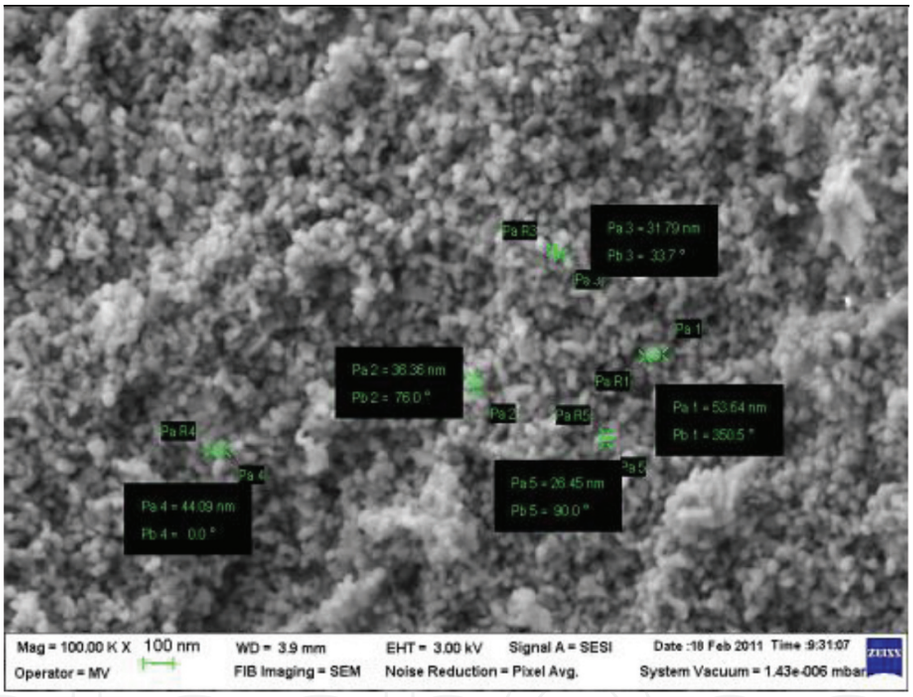

Figure 13. SEM images for sintering disc CeO_2-Y_2O_3.

3.4. The CO_2 gas sensing mechanism and gas sensors testing

The improved sensing response at CO_2 can be attributed to synergistic effects between Y_2O_3-doped CeO_2. In certain conditions such as high temperature, reduced state or pure CeO_2, lose some amount of oxygen and generate oxygen vacancies in accord with Eq. (7),

$$2CeO_2 \rightarrow Ce_2O_3 + O^{-}. \tag{7}$$

When CO_2 comes in contact with CeO_2-activated surface, this forms carbonates as a product through the participation of surface oxide ions in accordance with Eq. (8),

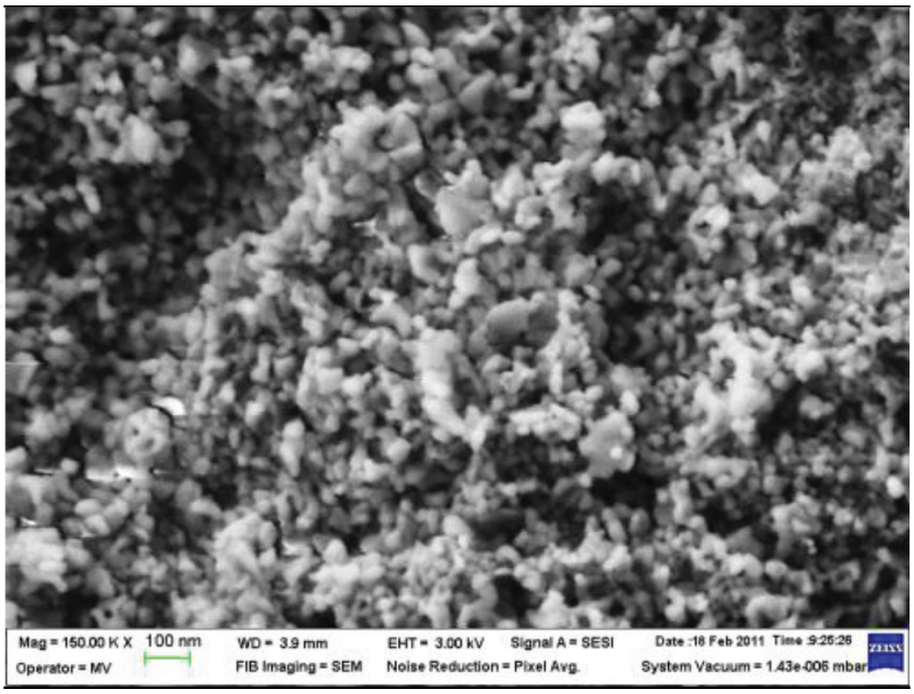

Figure 14. SEM images for oxidic powder CeO_2-Y_2O_3 calcined at 800°C for 2 hours.

$$O^{2-} + CO_2 \rightarrow CO_3^{2-}. \tag{8}$$

The carbonates disappear when they are exposed to oxidizing conditions [31]. The sensor characteristic was performed using test installation presented in **Figure 4**. The sensor was exposed at CO_2 atmospheres in the concentration range of 0–5000 ppm CO_2 in the climatic conditions: T = 20°C and two relative humidity testing 40% RH and 80% RH, respectively. The sensor functions at 135°C, temperature provided by the heating resistance (**Figure 9**, Pos. 7). **Figure 15** shows the variation of sensor voltage with the gas concentration. The characteristics show a slow linear decreasing of voltage with CO_2 concentration which allows an easy signal conditioning. In the concentration range 0–5000 ppm CO_2, the sensor presents a voltage variation as follows: 378.17–377.32 mV for T = 20°C, RH 40% and 377.11–376.61 mV for T = 20°C, RH 80%. The sensor data show a little dependence of voltage with relative humidity that makes usable in environment with high relative humidity. The sensitivity of the sensor was 0.3 V/ppm and the response time was less than 30 s [44].

3.5. Signal conditioning of the sensing element for CO_2 gas detection with Y_2O_3-doped CeO_2 sensitive material

The operational amplifier ADA4627-1, provided by analog devices (**Figure 16**) is a broadband and high precision amplifier. It is recommended in applications like "sensor conditioning" and electronic conditioning of the signal, due to its exceptional attributes: low noise, very low offset voltage, very high common-mode rejection ratio (CMMR) and very high slew rate. This operational amplifier combines the best "DC" features and very good dynamic characteristics

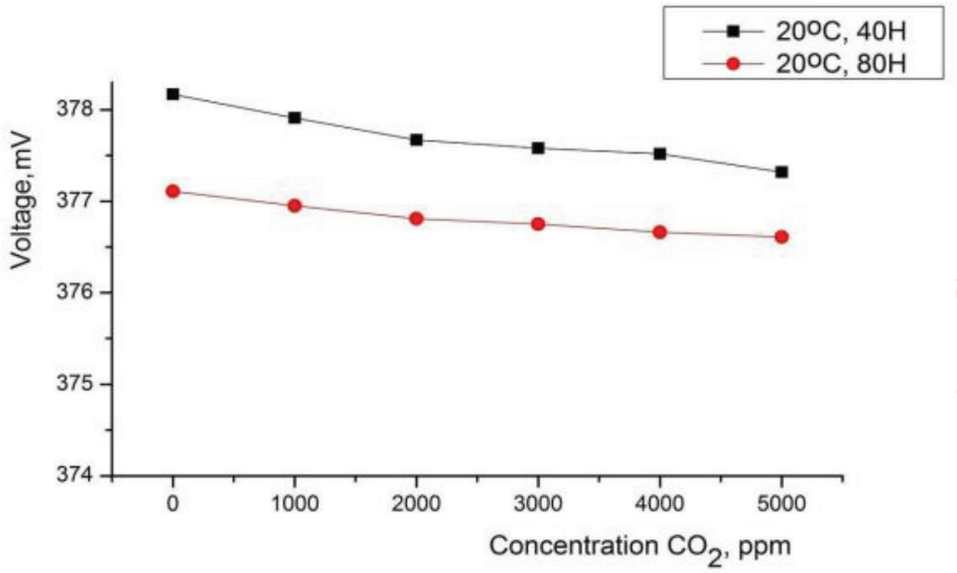

Figure 15. The sensor voltage function with CO_2 concentration, for $T = 20°C$ and two relative humidity testing 40% RH and 80% RH, respectively.

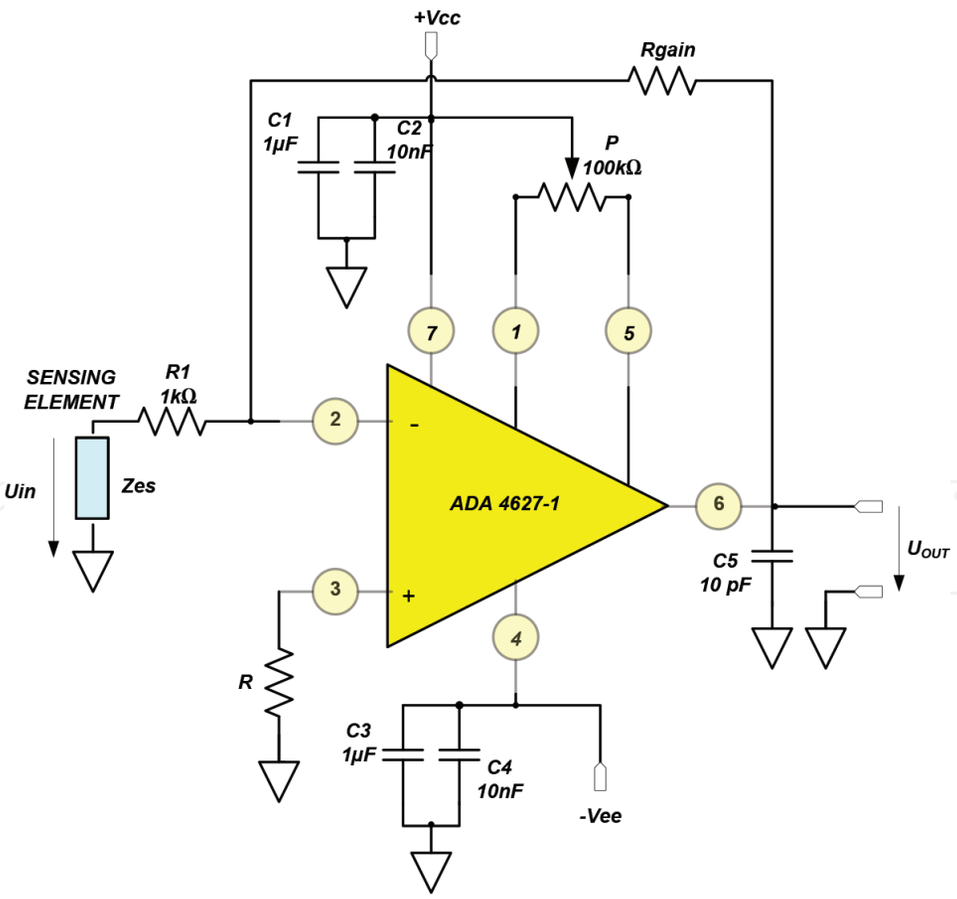

Figure 16. The electronic module for signal conditioning provided by sensing element, designing with ADA4627-1 analog devices.

[33], like: slew rate 60 V/μs; extended range of differential supply voltage: ±5 Vcc …. ± 15 Vcc; opn loop gain 120 dB; low offset voltage maximum 200 μV and the bias current: maximum 5 pA.

4. NO_2 gas sensor made with rGO-doped CeO_2 and CeO_2-doped rGO/ZnO

4.1. Synthesis of sensitive materials rGO-doped CeO_2 and CeO_2/rGO-doped ZnO

In order to study the CeO_2 sensor properties for NO_2 detection, two sets of sensitive materials for sensors was synthesized: (a) 1%rGO/CeO_2 nanocomposite as sensitive material to study the effect of rGO adding on the sensitivity and (b) 1%(wt. %)CeO_2 was added at 1%(wt.%) rGO/ZnO-nanocomposite, in order to study the effect of CeO_2 adding on the sensitivity.

A. Synthesis of 1%rGO/CeO_2: 1%(wt.%) rGO/CeO_2 nanocomposite was synthesized in situ by precipitation method using $Ce(NO_3)_3$ and NH_3 (25% conc) at 90°C and 30 min maturation time.

B. Synthesis of 1%CeO_2/1%rGO/ZnO: The 1%(wt.%)GO and 1%CeO_2 was mixed with ZnO in ethanol. The resulted powder after ethanol evaporation was heat treated at 150°C. The GO was synthesized by Hummers' modified method using as strong oxidant potassium permanganate (mass ratio C:oxidant = 1:3) in a solution of sodium nitrate and concentered sulfuric acid (1 g/150 ml) and graphite [45, 46].

4.2. Structural and morphological characterizations of the sensitive materials

UV-Vis diffuse reflectance spectroscopy measurements were performed a Jasco V-570 Spectrophotometer, Japan, equipped with integrating sphere for diffuse reflectance measurement mode and SPECTRALON reference as etalon, and bang gap software in order to evaluate the optical properties and band gap values of the CeO_2, doped CeO_2 with 1%rGO and doped 1%GO-ZnO nanocomposite with 1%CeO_2. The diffuse reflectance spectrum was converted in absorbance spectrum and presented in **Figure 17**. The band gap was calculated using Kubelka-Munk equation with associated plot $\sqrt{\alpha h\upsilon}$ versus photon energy E_g [eV], where α is extinction coefficient [cm^{-1}] and h is Planch constant $4.135x10^{-15}$ [eVs], υ is light frequency [s^{-1}] and wavelength [nm] [47–49]. The linearity coefficient was in all case bigger than 0.99.

In **Table 3**, the UV-Vis spectra parameters of UV-Vis measurements, for 1%rGO/CeO_2 and CeO_2 is also presented.

Legend: A_{abs} represents absorbance plasmon resonance (APR) and I represents intensity of APR.

The effect of doping of CeO_2 with 1%rGO leads to blue shift of APR presented in **Table 3** and **Figure 17** accompanied by the hyperchromic effect for both peaks, while the band gap are narrows, keeping the same characteristic shape of the ceria spectrum. The same effect—a blue shift has been described in literature for both TiO_2 aditived with GO and for ZnO aditived with

http://dx.doi.org/10.5772/intechopen.80801

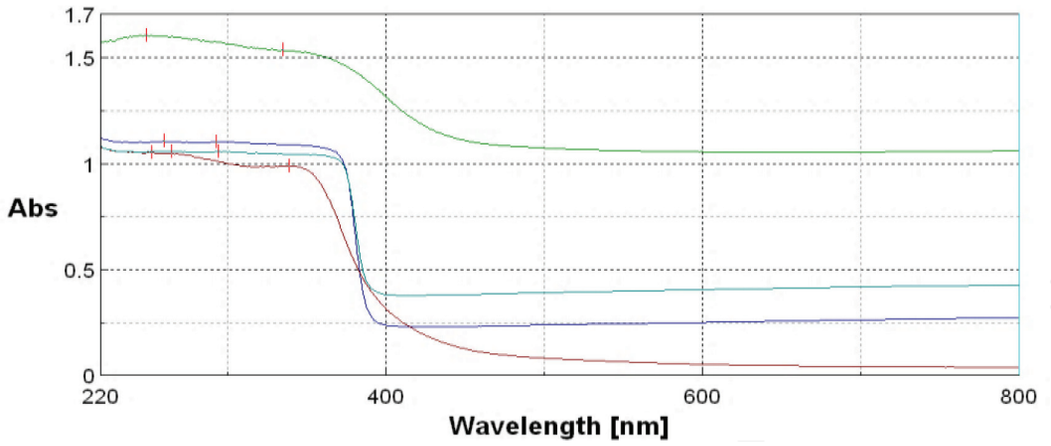

Figure 17. Diffuse reflectance UV-Vis spectroscopy spectra for CeO_2 (red), (1%CeO_2/1%rGO) ZnO (blue), 1%rGO/ZnO (lagun) and 1%rGO/CeO_2 (green).

Samples	$Abs_{max}1$	I1	$Abs_{max}2$	I2	Band gap, [eV]	
1%rGO/CeO_2	249	1.065	335	1.535	3.05	
	Blue shift	Hyper chromic effect	Blue shift	Hyper chromic effect	band gap narrowing	
CeO_2 -standard	252	1.051	339	0.99	theoretical	Commercial type
					3.19, Ref. [47]	3.16

Table 3. UV-Vis spectra parameters of UV-Vis measurements.

GO [50, 51]. The introduction of 1%GO(wt.%) in CeO_2 leads to a decrease in the effective optical band gap value from 3.16 eV to 3.05 eV, with a variation of 0.11 eV. This shows that the 1%GO(wt.%) acted as a band gap modifier [47–49, 52]. The same effect has been described in literature for the introduction of GO and related materials rGO in TiO_2 leads to a decrease in band gap [50]. Earlier, a lot of researchers attempt to tailor the properties of oxide semiconductors by using band gap modifiers and in this way to improve the catalytic, photovoltaic and sensing properties; this new trend is named bend gap engineering [47–49, 52]. Many researchers obtained a band gap narrowing after heat treatment of CeO_2 [52] and doping with different metals as Co [52], Gd [53], functionalized by different techniques [47], etc. Rare earth oxides present a high basicity related to ordinary oxide semiconductors such as TiO_2, WO_3, SnO_2 and ZnO, fast oxygen ion mobility and interesting catalytic properties which are important in gas sensing application [54–56]. **Table 4** presents UV-Vis spectra parameters of UV-Vis measurements for 1%CeO_2/1%rGO/ZnO and 1%rGO/ZnO.

In the case of doping with 1%(wt.%)CeO_2 of the 1%(wt.%)rGO/ZnO nanocomposite, the effect is the same, an increasing of APR accompanied by the hyperchromic effect with the preservation of the characteristic spectra shape. But in opposite with the first case of CeO_2 doped with 1%GO(wt.%), there is a decrease in effective optical band gap value from 3.24 to 3.19 eV, with a variation of 0.05 eV. This shows that the 1%CeO_2(wt.%) acted as a band gap modifier. The UV-Vis spectra present a strong absorption bands below 400 nm in UV region for the nanocomposites with the main component ZnO which are attributed to ZnO NP. The APR of ZnO nanocomposites are

Samples	$Abs_{max}1$	I1	$Abs_{max}2$	I2	Band gap, [eV]
1%CeO_2/1%rGO-ZnO	260	1.104	293	1.103	3.19
	Blue shift	Hyper chromic effect	Blue shift	Hyper chromic effect	Band gap narrowing
1%rGO-ZnO-etalon	265	1.059	294	1.056	3.25
ZnO	376 Ref. [60]	—	—	—	Theoretic 3.37 Ref.: [48], [57–60]

Legend: A_{abs} represents absorbance plasmon resonance (APR) and I represents intensity of APR.

Table 4. UV-Vis spectra parameters of UV-Vis measurements for 1% CeO_2/1%rGO/ZnO and 1%rGO/ZnO.

lower, in generally, than the absorption band of bulk ZnO (373 nm) that had a wide direct band gap at room temperature of 3.37 eV [48, 57–60]. CeO_2 adding on ZnO nanocomposite surface leads to a significant increase of the absorption in the UV light spectrum and decrease in the visible light spectrum. Based on the above results, UV-Vis and transformed Kubelka–Munk function plots suggested that are necessary energy for generation of electrons in conduction bands and holes in valence bands is smaller for the doped 1%rGO/CeO_2 than the CeO_2, this makes the doped CeO_2 more reactive and sensitive. Other researchers tried to improve the sensing properties of ZnO sensor, for ethanol detection, by adding noble metals such as Pd [61], Pt [62] and Au [63], other metals such as Al, In, Cu, Fe and Sn [64], oxides as TiO_2 [65], CuO [66], CoO [67], RuO_2 [68] and SnO_2 and not in the end Ce and CeO_2 [55]. There is a current practice to use band gap modifiers. Many researchers use a band gap modifier in order to improve the functional properties of nanocomposite based on semiconductors oxides. The functional properties are ranging from the photocatalytic properties, sensitivity and selectivity for different sensor types, catalysts and others [52]. Raman spectroscopy measurements was performed with Raman dispersive spectrometry–LabRam HR Evolution, Horiba Jobin Yvone, France, equipped with Laser wave 532 nm, acquisition time 5 s, 10 accumulation, 0.1% laser power, used in order characterized the order-disorder degree in the synthetized nanocomposite. **Figure 18** shows the RAMAN spectra for CeO_2 and rGO/CeO_2.

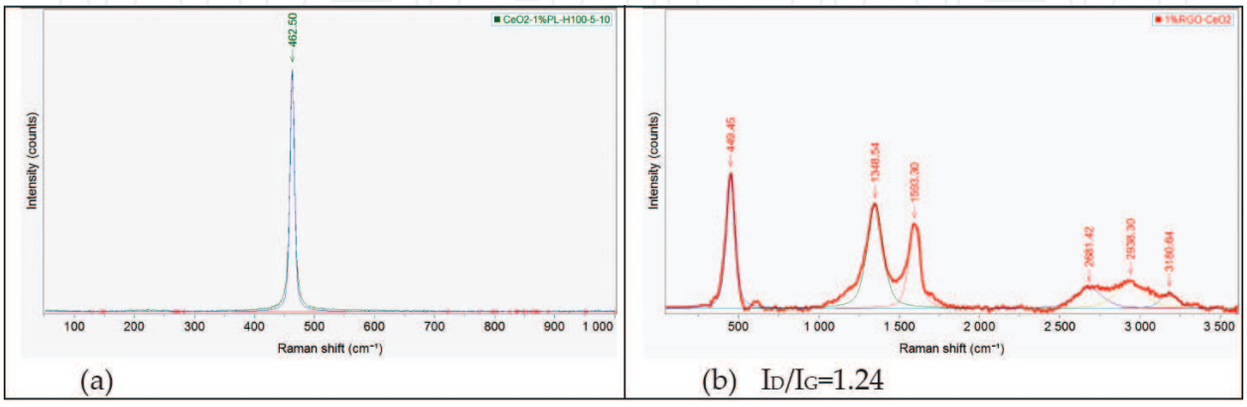

Figure 18. Raman spectra for CeO_2 powder (a) and synthetized 1%rGO/CeO_2 (b).

http://dx.doi.org/10.5772/intechopen.80801

Figure 18(a) presents the Raman spectrum of CeO_2 powder which reveals a peak situated at 462.5 cm^{-1} characteristic for CeO_2, corresponding to the Raman active modes F_{2g} for Ce–O symmetric breathing mode of oxygen atoms around the Ce atoms [49]. **Figure 18(b)** shows the Raman spectrum of 1%rGO/CeO_2 with characteristic peak of ceria at 449 cm^{-1} corresponding to the Raman active modes of CeO_2 and characteristics graphene oxide peaks [69] at 1348.54 cm^{-1} (D band), 1593.30 cm^{-1} (G band), 2681.42 cm^{-1} (2D band), 2938.30 cm^{-1} (2D + D′ band) and 3180.64 cm^{-1} (G + D′ band). According to the Raman line, broadening is equivalent with lattice constant cell crystallographic parameter a_o of CeO_2 can be estimated by Eq. (9) [49], with 0.9 nm for CeO_2 powder and 0.43 nm for the CeO_2 from the 1% rGO-CeO_2 nanocomposite. The characteristic peak of CeO_2 was shifted with 13.05 cm^{-1} at lower wave number as a doping effect of 1%rGO.

$$FW\left[\mathrm{cm}^{-1}\right] = 10 + \frac{124,7}{d}\ [\mathrm{nm}] \tag{9}$$

where the FW is full wide at half-maximum of the Raman active mode F_{2g} and d is the diameter particle in nm. **Figure 19(a)** shows the Raman spectrum of GO with characteristic peaks of graphene oxide peaks at 1347.96 cm^{-1} (D band), 1595.33 cm^{-1} (G band), 2681.77 cm^{-1} (2D band), 2914.68 cm^{-1} (2D + D′ band) and 3196.75 cm^{-1}(G + D′ band). **Figure 19(b)** shows the Raman spectrum of 1%CeO_2/1%rGO/ZnO with characteristic peaks of graphene oxide peaks at 1350.87 cm^{-1} (D band), 1605.74 cm^{-1} (G band), 2684.22 cm^{-1} (2D band) and characteristic peaks of ZnO and active modes F_{2g}, CeO_2 (462.79 cm^{-1}), where the I_D/I_G can be used to evaluate quantitative the crystallinity/disorder degree and are varying between 1.05 and 1.24, lower value indicates the less defects in graphitic structure [69]. **Figure 20** shows the morphologies for the three sensitive materials reveals for (a) CeO_2 was evidentied a polycrystalline structure, for (b) CeO_2/rGO - the micrographic image presents a 3-D layered structured of GO mixed with small polycrystalline particles of ceria and for (c) CeO_2/rGO/ZnO was evidentied a mixed polycrystalline structure of preponderant small particles of wurtzite hexagonal types ZnO and minor faces of cubic CeO_2 and carbon faces.

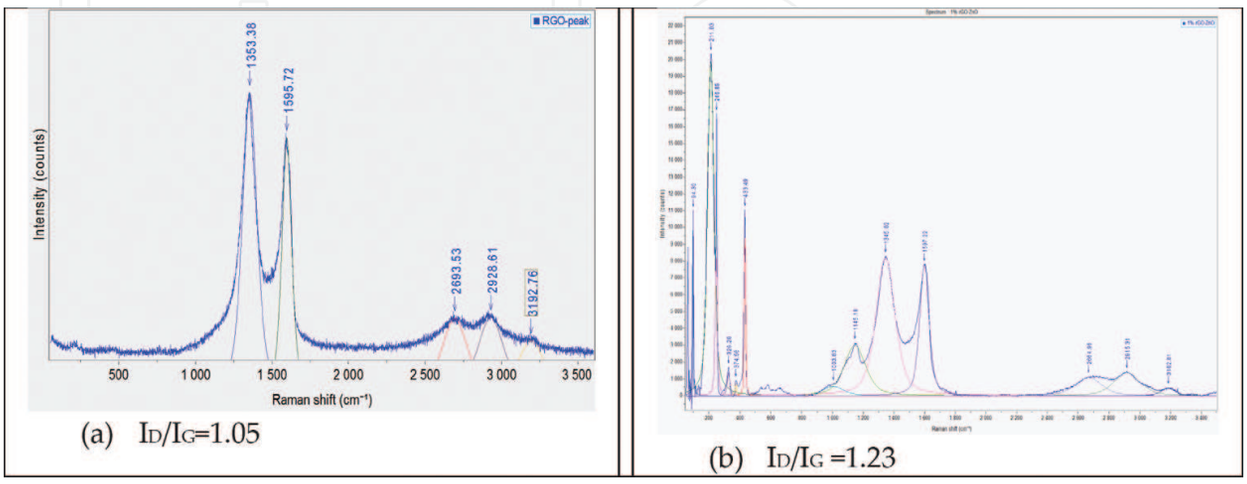

Figure 19. Raman spectra for rGO (a) and synthetized 1%CeO_2/1%rGO/ZnO (b).

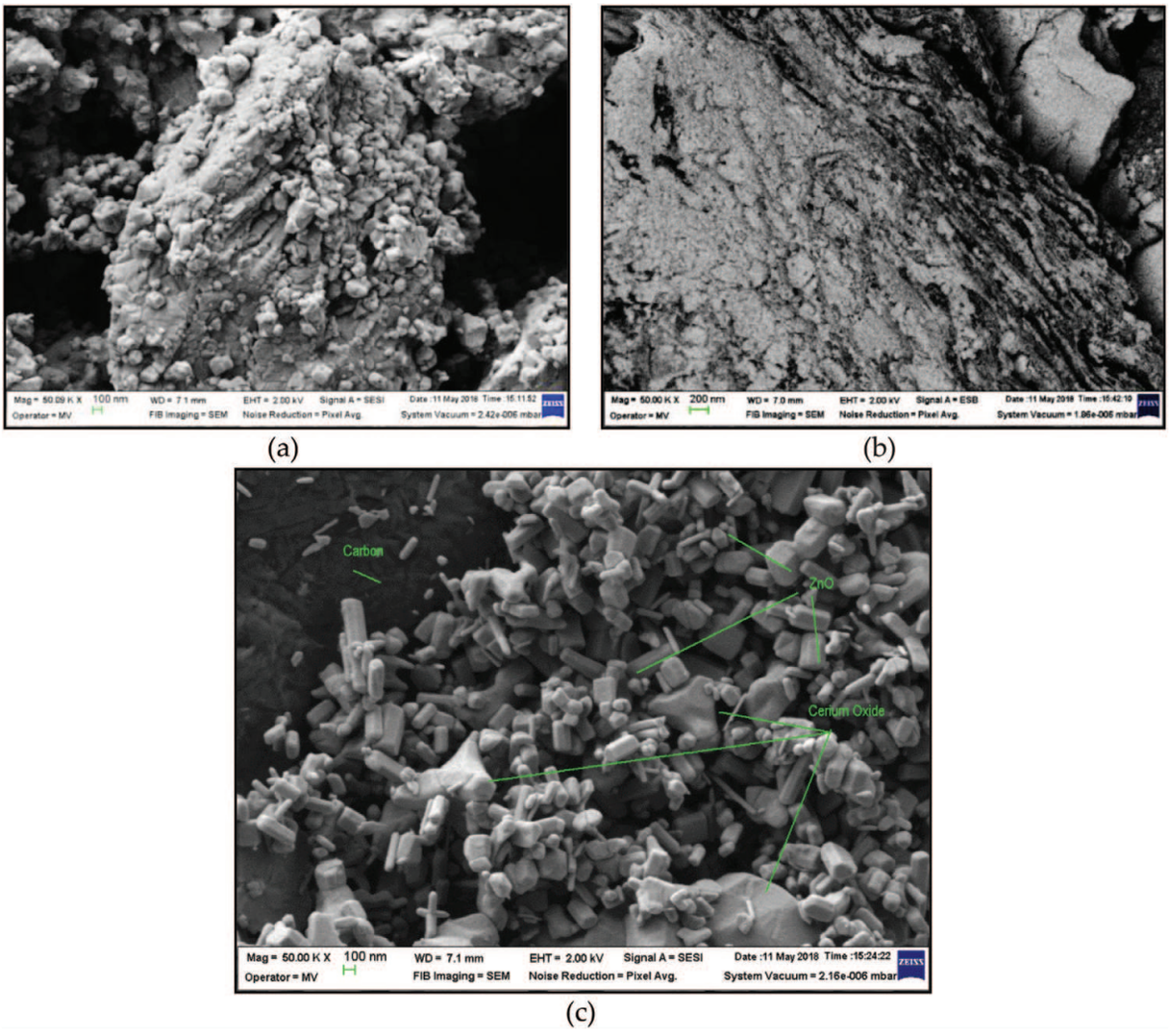

Figure 20. SEM images for: (a) CeO_2; (b) CeO_2/rGO; (c) CeO_2/rGO/ZnO.

4.3. The construction of the sensing element for NO_2 gas detection designed with rGO-doped CeO_2 and CeO_2-doped rGO/ZnO sensitive material

The sensor module is constituted from printed circuit board (PCB), substrate with interdigitated Ag array electrode deposed by photolitografic technology and the sensitive material in amounts 15–20 mg was deposited on surface electrode. The active area for sensitive material was 10 mm × 0.5 mm, **Figure 21(a)** and **(b)**.

4.4. The NO_2 gas sensing mechanism

In metal oxide semiconductor gas sensors, the resistance is measured as a function of the gas concentration. Generally, this devices function at elevated temperature between 200 and 600°C in air. The grain of metal oxide is covered by adsorbed oxygen molecules. Oxygen molecules present the character of electronegativity, they extract electrons from the conduction band of

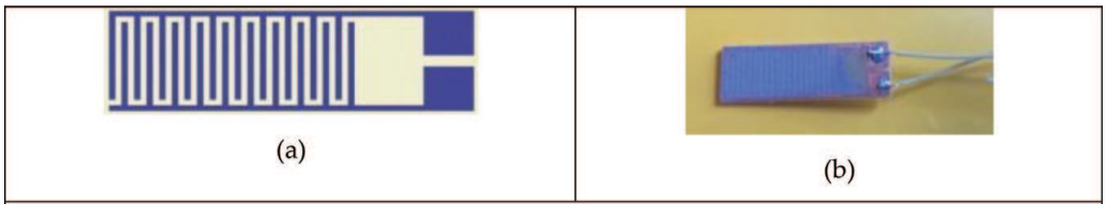

Figure 21. The NO_2 gas sensing element structure (a) PCB substrate with interdigitated Ag array electrode; (b) the sensing element made with PCB substrate and sensitive material deposed on surface electrode.

metal oxide causing the formation of oxygen ions O_2^-, O^-, O^{2-}, adsorbed at the surface of metal oxide. Since electrons are removed from the metal oxide, the concentration of free charge carriers is reduced forming a depletion layer at grain boundaries. The surface reactions can be written according with Eqs. (10–12):

$$O_{2(gas)} + e^- \rightarrow O_2^-(ads) \tag{10}$$

$$½O_2(gas) + e^- \rightarrow O^-(ads) \tag{11}$$

$$O^- + e^- \rightarrow O^{2-}(ads) \tag{12}$$

As is it known, nitrogen oxides specify as NO_x have the character of oxidizing gases with very high electron affinity 2.28 eV as compared with oxygen 0.43 eV. The NO_x molecules interact with the surface of metal oxide through surface adsorbed oxygen ions, thus increasing the potential barrier at grain boundaries. The redox reactions taking place on the surface of a metal oxide can be written according with Eqs. (13–14) [70].

$$NO/NO_{2(gas)} + e^- \rightarrow NO^-/NO_2^-(ads) \tag{13}$$

$$NO/NO_2(gas) + O_2^-(ads) \rightarrow NO^-/NO_2^-(ads) + O_2(gas) \tag{14}$$

As result, the thickness and resistance of the depletion layer increase and resistance change is reversible at operating temperature [70]. The oxygen vacancies can significantly enhance the adsorption of oxygen molecules and electrons will transfer from the oxygen vacancies from CeO_2 to the oxygen molecules, resulting in more oxygen species (especially O^{2-}). These oxygen species will react with NO_2, resulting in an abrupt change in the conductivity of the sensor [71]. The graphene sheets by their good properties as: high surface area 2630 m^2/g, thermal conductivity in the range of 3000–5000 W/mK at room temperature carrier mobility up to 200,000 cm^2/Vs [72], electrical conductivity of 7200 S/m [73], coming from their structure two-dimensional (2D) single atom layer is used in gas sensing and in the composite leads to increase of the electrical conductivity of CeO_2 and thus improve the performance to gas sensing room temperature [71].

4.5. The NO_2 gas sensors testing and sensing characteristics

The sensors with sensitive materials 1%rGO-doped CeO_2, and 1% CeO_2/1%rGO-doped ZnO were tested in NO_2 atmosphere in concentrations 5 and 10 ppm. The gas testing was effected

with testing installation presented in **Figure 4**. The gas testing was performed in order to establishment of the sensitivity sensors and response time. The sensor sensitivity was expressed in accord with Eq. (15), as the ratio of resistance in air to that in target gas, in this case NO_2,

$$S = \frac{Ra}{Rg} \tag{15}$$

where *Ra* is the resistance of sensor in air and *Rg* is the resistance of sensor in gas.

The response time is expressed by formula:

$$Ra - 90\%x(Ra - Rg) \tag{16}$$

Notations are the same with Eq. (15) [28]. Having the resistance values, from the graph, the response time can be determined. **Figure 22** shows the resistance variation with time exposure gas and **Figure 23** shows the sensitivity (response) for sensing element with time exposure gas for two sensitive material: 1%rGO/CeO_2 and 1%CeO_2/1%rGO/ZnO. All the characteristics are considered for the 1 hour time exposure. Since the resistance of sensors decreases sharply, for a good view we opted for a semilogarithmic scale representation of resistance and sensors response with exposure time. The decreases of resistance denotes a character of type p semiconductors for both sensitive materials in oxidant gas like NO_2, character given by reduced graphene oxide which is a semiconductor type p.

The sensors performances can be resumed in **Table 5**.

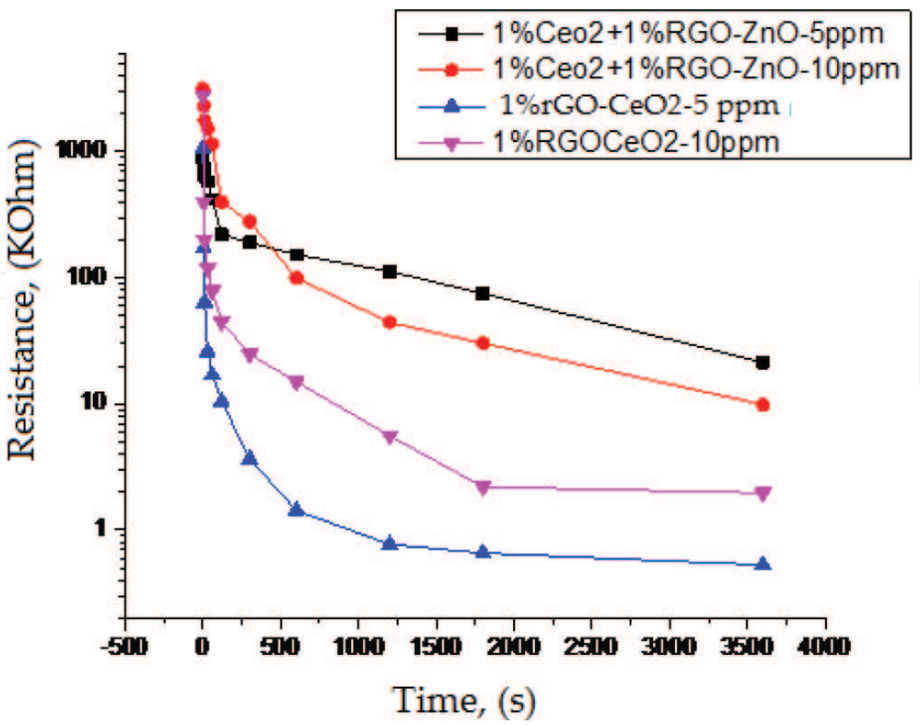

Figure 22. Resistance variation function with time.

http://dx.doi.org/10.5772/intechopen.80801

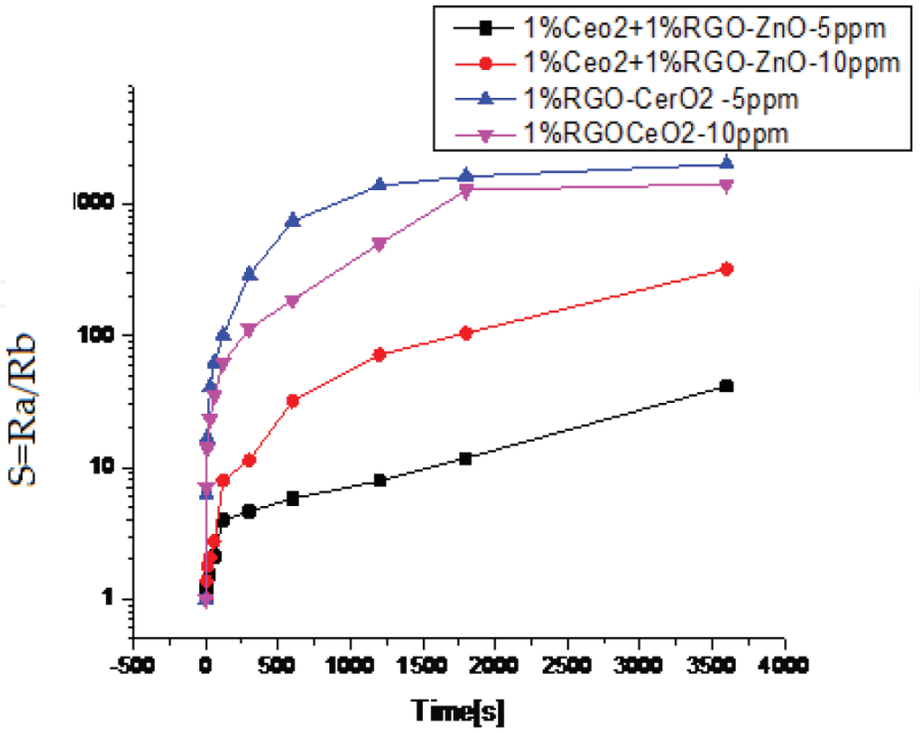

Figure 23. The sensitivity variation function with time.

Sensitive material	Concentration NO_2, [ppm]	Resistance in air, [kΩ]	Resistance in gas, [kΩ] (after 3600 s exposure)	Sensitivity, *Ra/Rg*	Response time, [s]
1%rGO/CeO_2	5	1060	0.53	2000	2.5
1%CeO_2/1%rGO/ZnO	5	885	21.43	41.29	2.8
1%rGO/CeO_2	10	2800	1.54	1818	3.5
1%CeO_2/1%rGO/ZnO	10	3180	9.9	321.2	2.2

Table 5. The characteristics of sensors with sensitive materials 1%rGO/CeO_2 and 1%CeO_2/1%rGO/ZnO.

Analyzing the obtained results, it can be concluded that the both sensitive materials show the good performance at NO_2 exposure at room temperature. However, the sensitive material composed by 1%rGO/CeO_2 presents very good sensitivity at NO_2 exposure for 5 and 10 ppm concentrations of 2000 and 1818 and very short response time of 2.5and 3.5 s. Thus, sensitive materials with CeO_2 in majority concentration in matrix with reduced oxide graphene presents the best performance at NO_2 detection, face to sensitive materials 1%CeO_2/1%rGO/ZnO where ZnO is majority and are a promising sensitive materials for NO_2 detection.

4.6. Signal conditioning of the sensing element for NO_2 gas detection designed with rGO-doped CeO_2 and CeO_2-doped rGO/ZnO sensitive material

Resistance of sensor sensing element ES, R + ΔR, **Figure 24** may vary from less than 10 kΩ to several hundred kΩ, depending on the design of the sensor and the physical environment to

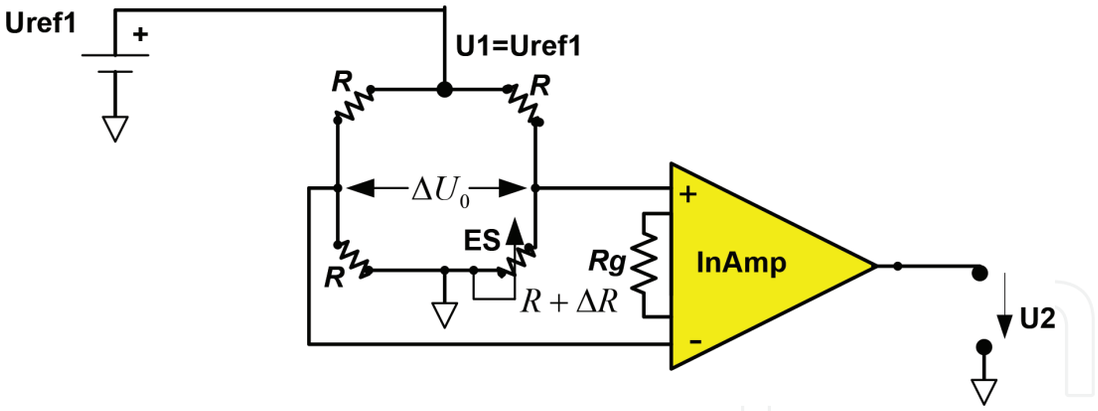

Figure 24. Schematic of the electronic block for signal conditioning generated by the sensing element.

be measured. The sensing element ES of the NO_2 gas sensor is disposed in one of the Wheatstone bridge arms and shows the resistance R for a NO_2 concentration of zero ppm. The resistances of resistors disposed in all of other branches of the bridge show the same value, namely R. A DC voltage excitation source U1 is connected to one of the bridge diagonals [74].

If the gas concentration of NO_2 is zero ppm, the sensing element ES shows the resistance R. The Wheatstone bridge is in this case at equilibrium so that the voltage measured on the other diagonal of the bridge is 0 V. Variation of NO_2 gas concentration in the range from zero ppm to 10 ppm causes a voltage variation with ΔU_0, which can be measured on the other diagonal of the bridge. The voltage variation up to ΔU_0 is given by the relation (17):

$$\Delta U_0 = \frac{U1}{2}\left[\frac{\frac{\Delta R}{2}}{R + \frac{\Delta R}{2}}\right] \tag{17}$$

The operational amplifier that can be used with the best performance is instrumentation type amplifier (in-amp), "resistor programmable" (**Figure 24**). Considering the transfer function of the electronic amplifier module and taking into account the relation (17), we obtain [74]:

$$U2 = \frac{U1}{2}\left[\frac{\frac{\Delta R}{2}}{R + \frac{\Delta R}{2}}\right] A = K\left[\frac{\frac{\Delta R}{2}}{R + \frac{\Delta R}{2}}\right], \tag{18}$$

where A is the amplification factor, depending on the R_g resistance value and $K = \frac{U1}{2}A$, is a constant. In-amps such as the AD620 family, the AD623 and AD627, Analog Devices type can be used in single (or dual) supply bridge applications.

4.6.1. Realization of the continuous U1 excitation voltage source

The continuous U1 excitation voltage source is made using a D/A digital/analog converter, a Uref reference voltage and an operational amplifier (OA) (**Figure 25**). Thus, depending on the values set for the least significant bit (LSB) up to the most significant bit (MSB), the resulting word can establish a desired U1 continuous excitation voltage. **Figure 25** shows the schematic of the electronic block for the U1 excitation voltage source.

http://dx.doi.org/10.5772/intechopen.80801

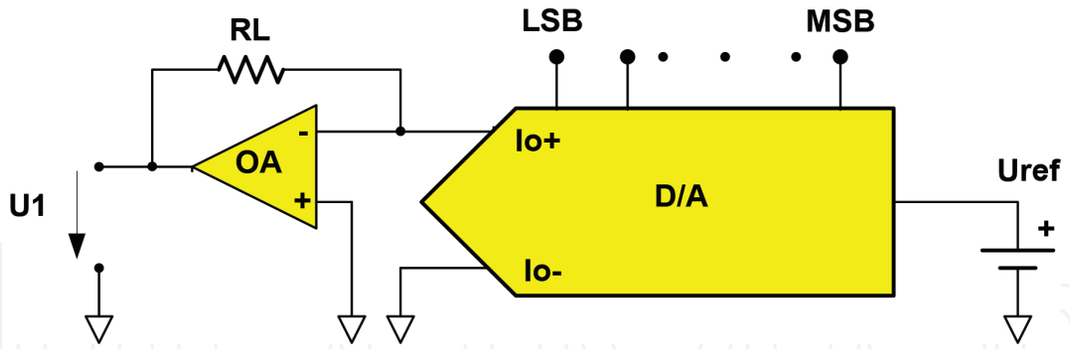

Figure 25. Schematic of the electronic block for the U1 excitation voltage source.

4.6.2. Bridge-linearization electronic circuit

Schematic of the electronic linearization block of the signal generated by the Wheatstone bridge, via an operational amplifier, in-amp uses an analog multiplier [75], AD 534 or AD 734, produced by analog devices (**Figure 26**). The transfer function associated with the AD 534 or AD 734 analog multiplier is written [76, 77]:

$$W = A_0\left\{\frac{(X1 - X2)(Y1 - Y2)}{SF} - (Z1 - Z2)\right\} \tag{19}$$

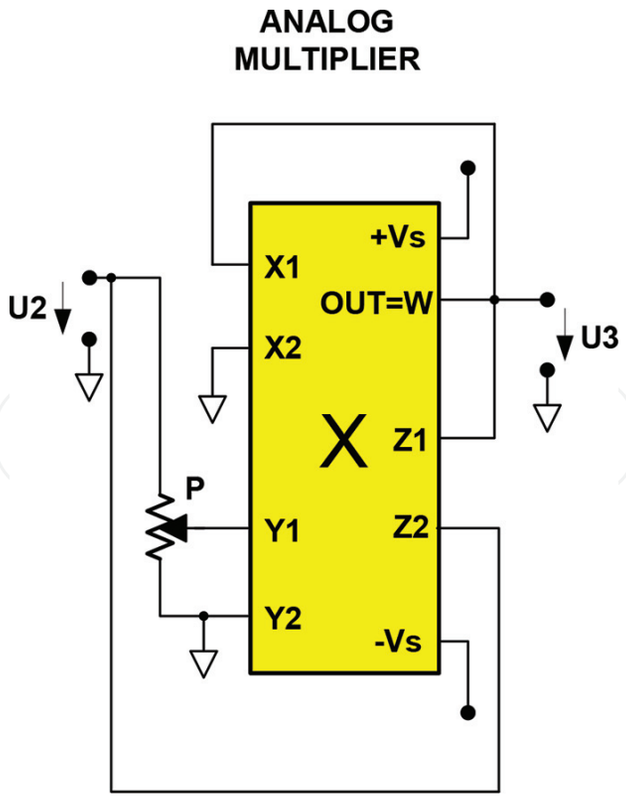

Figure 26. Schematic of the electronic linearization block of the signal generated by the Wheatstone bridge, via an operational in-amp instrumentation amplifier.

where A_0 is the open loop gain, X1, X2, Y1, Y2, Z1 and Z2 represent the inputs of the analog multiplier, SF a scale factor, typically SF = 10 V and W = OUT, according to **Figure 26**.

Since $A_0 \rightarrow 72$ dB can be considered as $W/A_0 \rightarrow 0$ and the relation (19) becomes:

$$(X1 - X2)(Y1 - Y2) = SF(Z1 - Z2) \tag{20}$$

Since Z1 = W it is obtained:

$$W = \frac{(X1 - X2)(Y1 - Y2)}{SF} + Z2 \tag{21}$$

Since Z2 = U2, Y1-Y2 = βU2, $0 \leq \beta < 1$, X2 = 0 and X1 = Z1 = W=U3, according to **Figure 26**. Finally,

$$U3 = W = \frac{U2}{1 - \frac{\beta U2}{SF}} \tag{22}$$

is obtained

The relation (6) together with the relation (2) represents the calculation method regarding the linearization of the signal generated by the Wheatstone bridge, via an operational in-amp instrumentation amplifier.

4.6.3. Resulting structures for the electronic block for signal conditioning generated by the sensing element

By considering the three previously analyzed electronic blocks, the electronic block for signal conditioning generated by the sensing element is obtained. **Figure 27** shows the schematic of

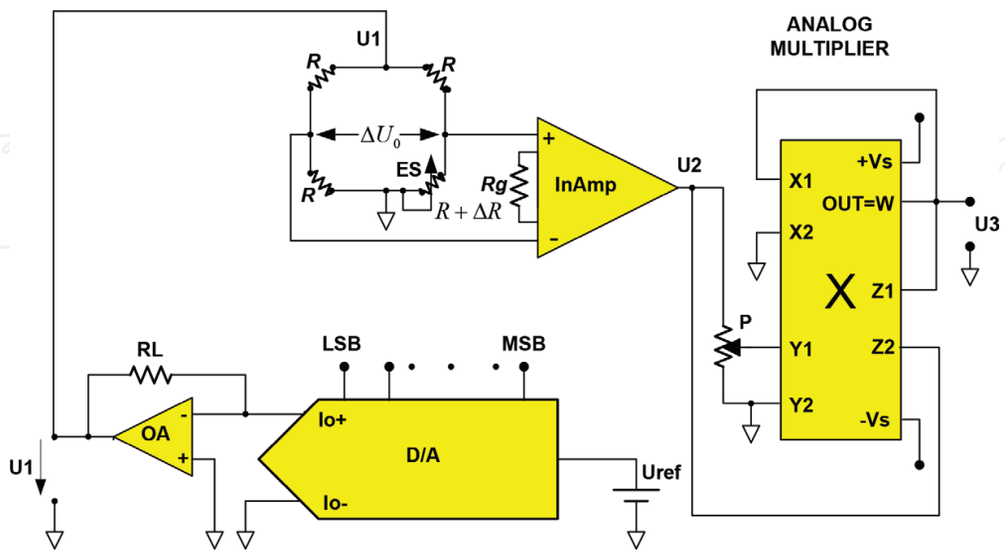

Figure 27. Schematic of the electronic block for signal conditioning generated by the sensing element, single supply bridge applications.

http://dx.doi.org/10.5772/intechopen.80801

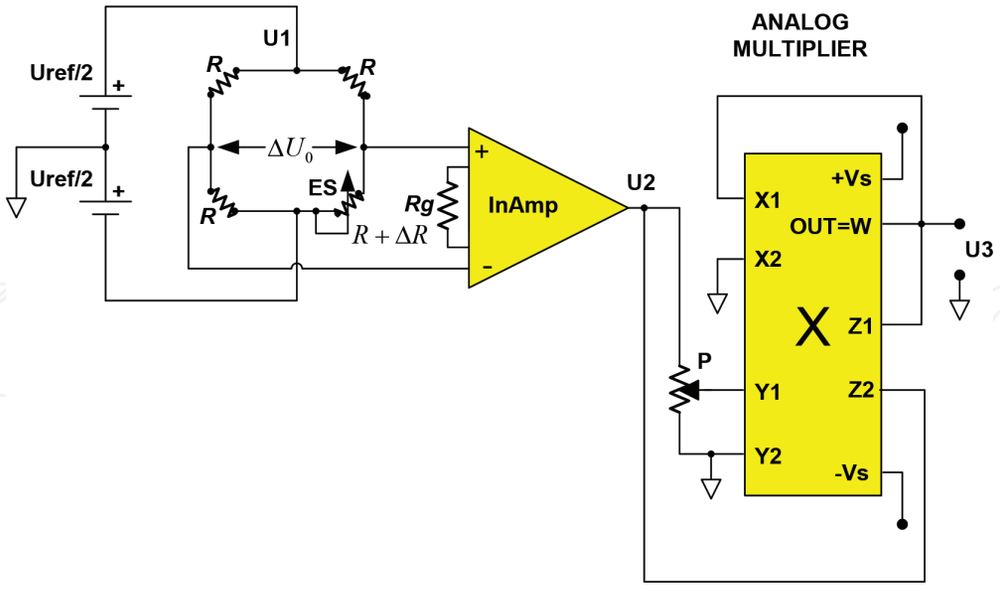

Figure 28. Schematic of the electronic block for signal conditioning generated by the sensing element, dual supply bridge applications.

the electronic block for signal conditioning generated by the sensing element, single supply bridge applications.

It is possible to reconfigure circuits so as to improve the performance in terms of reduces the dc common-mode voltage to zero. **Figure 28** shows how the use of split U1 tension in order to reduce the dc common-mode voltage to zero.

An isolation amplifier can be useful for this application, with respect to the signal-conditioning, so that it does not exist galvanic connections between the bridge and grounded instrumentation circuitry.

5. Conclusions

Cerium, by its unique electronic configuration ([Xe] $4f^2 6s^2$) and by the two common valence states Ce^{3+} and Ce^{4+} allowing a redox reaction between them which gives CeO_2 excellent chemical and physical properties, is used in many applications, like as: three-way catalytic reactions to eliminate toxic automobile exhaust, the low-temperature water gas shift reaction, oxygen permeation membrane systems for fuel cells as well as gas sensors. For gas sensing applications, several sensitive elements based on CeO_2 were tested to determine both this detection function as well as this performances:

- By doping the CeO_2 with oxides semiconductor, for example, Nb_2O_5 introduced in CeO_2 structure, the following mechanism is triggered: Nb^{5+} ions initiate the reduction of Ce^{4+} to Ce^{3+} resulting in the formation of oxygen vacancies with consequences in increasing the sensitivity.
- The ionic conductivity of CeO_2 is improved by doping with rare earth oxides such as Sm_2O_3, Gd_2O_3 and Y_2O_3. The size of conductivity for doped ceria depends on the ionic

radius of the doping ion. Therefore, the introduction of trivalent ions in ceria leads to the production of anion vacancies which may enhance catalytic and gas sensing.

- CO_2 detection using sensitive material based on mixed binary oxide CeO_2-Nb_2O_5 in ratio 97%/3%, for 10,000 ppm CO_2 at the 25, 50 and 70°C chamber test temperature, the sensor was developed voltage values of 48, 50 and 770 mV.
- CO_2 detection with Y_2O_3-doped CeO_2 molar ratio CeO_2/Y_2O_3 = 4:1 with characteristics: the CO_2 concentration in the range of 0–5000 ppm, function temperature 135°C, climatic conditions T = 20°C, 40% RH and 80% RH, voltage values 378.17–377.32 mV for T = 20°C, 40% RH and 377.11–376.61 for T = 20°C, 80% RH. Sensitivity is 0.3 V/ppm and response time 30 seconds;
- Sensitive materials based on 1%rGO/CeO_2 and 1%CeO_2/1%rGO/ZnO was analyzed with UV-Vis spectroscopy showing that a decreasing of band gap of CeO_2 in matrix with rGO from 3.19 eV at 3.05 eV what allows for sensor to function at room temperature. The sensors were tested for 5 and 10 ppm NO_2 obtaining the sensitivities of 2000 and 1818, response times of 2.5 and 3.5 s for sensitive material 1%rGO/CeO_2 and sensitivities of 41.29 and 321.2, response times of 2.8 and 2.2 s for sensitive material 1%CeO/rGO/ZnO. The sensitive materials made so that the matrix in which CeO_2 is in majority presents the best performance.
- Also, the sensing mechanism in CO_2 and NO_2 detection was discussed.

Based on these results, it can be stated that CeO_2 is a good candidate in gas sensors applications.

Acknowledgements

The research was performed with the support of Ministry of Research and Innovation, NUCLEU Programme Research Projects - Romania, Contract PN18240301/2018, "Sensors and electronic actuators based on new active materials", and UEFISCDI, Program 2 - Romania, Contract 4SOL/2017, "Development and implementation of modern solutions for gas turbine propulsion systems and their associated systems".

Conflict of interest

No conflict of interest exists with regard to this chapter.

Author details

Lucian Pîslaru-Dănescu*, Gabriela Telipan, Ioana Ion and Virgil Marinescu

*Address all correspondence to: lucian.pislaru@icpe-ca.ro

National Institute for Research and Development in Electrical Engineering ICPE-CA, Bucharest, Romania

References

[1] Song S, Wang X, Zhang H. CeO_2-encapsulated noble metal nanocatalysts: Enhanced activity and stability for catalytic application-review. NPG Asia Materials. 2015;**7**:e179. DOI: 10.1038/am.2015.27

[2] Babitha KK, Sreedevi A, Priyanka KP, Sabu B, Vargheze T. Structural characterization and optic studies of CeO_2 nanoparticles synthesized by chemical precipitation. Indian Journal of Pure & Applied Physics. 2015;**53**:596-603

[3] Melchionna M, Fornasiero P. The role of ceria-based nanostructured materials in energy applications. Materials Today. 2014;**17**(7):349-357. DOI: 10.1016/j.mattod.2014.05.005

[4] Hadi A, Yaacob II. Synthesis of PdO/CeO_2 mixed oxides catalyst for automotive exhaust emissions control. Catalysis Today. 2004;**96**(3):165-170. DOI: 10.1016/j.cattod.2004.06.118

[5] Andreeva D, Idakiev V, Tabakova T, Ilieva L, Falaras P, Bourlinos A, et al. Low-temperature water-gas shift reaction over Au/CeO_2 catalysts. Catalysis Today. 2002;**72**(1-2):51-57. DOI: 10.1016/S0920-5861(01)00477-1

[6] Kharton V, Figueiredo FM, Navarro L, Naumovich EN, Kovalevsky AV, Yaremchenko AA, et al. Ceria-based materials for solid oxide fuel cells. Journal of Materials Science. 2001;**36**:1105-1117. DOI: 10.1023/A:1004817506146

[7] Ansari SA, Khan MM, Ansari MO, Lee SKJ, Cho MH. Band gap engineering of CeO_2 nanostructure using an electrochemically active biofilm for visible light applications. RSC Advances. 2014;**4**:16782-16791. DOI: 10.1039/c4ra00861h

[8] Prabaharana DMDM, Sadaiyandib K, Mahendran M, Sagadevand S. Structural, optical, morphological and dielectric properties of cerium oxide nanoparticles. Materials Research. 2016;**19**(2):478-482. DOI: 10.1590/1980-5373-MR-2015-0698

[9] Shi H, Hussain T, Ahuja R, Kang TW, Luo W. Role of vacancies, light elements and rare-earth metals doping in CeO_2. Scientific Reports. 2016;**6**:31345. DOI: 10.1038/srep31345

[10] Alla SK, Kollu P, Singh Meena S, Poswal HK, Prajapat CL, Mandal RK, et al. Investigation of magnetic properties for Hf4+ substituted CeO_2 nanoparticles for spintronic applications. Journal of Materials Science: Materials in Electronics. 2018;**29**(12):10614-10623. DOI: 10.1007/s10854-018-9125-x

[11] Kumar E, Selvarajan P, Muthura D. Synthesis and characterization of CeO_2 nanocrystals by solvothermal route. Materials Research. 2013;**16**(2):269-276. DOI: 10.1590/S1516-14392013005000021

[12] Sun C, Li H, Zhang H, Wang Z, Chen L. Controlled synthesis of CeO_2 nanorods by a solvothermal method. Nanotechnology. 2005;**16**:1454-1463. DOI: 0957-4484/05/091454

[13] Laberty-Robert C, Long JW, Lucas EM, Pettigrew KA, Stroud RM, Doescher MS, et al. Sol−gel-derived ceria nanoarchitectures: Synthesis, characterization, and electrical properties. Chemistry of Materials. 2006;**18**(1):50-58. DOI: 10.1021/cm051385t

[14] Yang H, Zhang K, Shi R, Tang A. Sol–gel synthesis and photocatalytic activity of CeO_2/TiO_2 nanocomposite. Journal of American Ceramic Society. 2007;**90**(5):1370-1374. DOI: 10.1111/j.1551-2916.2007.01540.x

[15] Shah N, Bhangaonkar K, Pinjari DV, Mhaske ST. Ultrasound and conventional synthesis of CeO_2/ZnO Nanocomposites and their application in the photocatalytic degradation of Rhodamine B dye. Journal of Advances in Nanomaterials. 2017;**2**(3):133-145. DOI: 10.22606/jan.2017.23001

[16] Liu K, Zhong M. Synthesis of monodispersed nanosized CeO_2 by hydrolysis of the cerium complex precursor. Journal of Rare Earth. October 2010;**28**(5):680-683. DOI: 10.1016/S1002-0721(09)60178-2

[17] Jayakumar G, Albert Irudayaraj A, Dhayal Ra A. Particle size effect on the properties of cerium oxide (CeO_2) nanoparticles synthesized by hydrothermal method. Mechanics Materials Science & Engineering. 2017;**9**(1):127-131. DOI: 10.2412/mmse.3.4.481.openaccesww.mmse.xyz

[18] Zhou YC, Rahaman MN. Hydrothermal synthesis and sintering of ultrafine CeO_2 powders. Journal of Materials Research. 1993;**8**(7):1680-1686. DOI: 10.1557/JMR.1993.1680

[19] Mazaheri M, Hassanzadeh-Tabrizi SA, Aminzare M, Sadrnezhaad SK. Synthesis of CeO_2 nanocrystalline powder by precipitation method. Materiały Ceramiczne/Ceramic Materials. 2010;**62**(4):529-532, www.ptcer.pl/mccm

[20] Sathyamurthy S, Leonard KJ, Dabestani RT, Parans Paranthaman M. Reverse micellar synthesis of cerium oxide nanoparticles. Nanotechnology. 2005;**16**(9):1960-1964. DOI: 10.1088/0957-4484/16/9/089

[21] Schubert D, Dargusch R, Raitano J, Chan S-W. Cerium and yttrium oxide nanoparticles are neuroprotective. Biochemical and Biophysical Research Communications. 2006;**342**: 86-91, www.elsevier.com/locate/ybbrc

[22] Zhou Y. Nanostructured cerium oxide based catalysts: Synthesis, physical properties and catalytic performance. A Dissertations, and Theses. Chemistry Department, University of Nebraska-Lincoln Digital Commons University of Nebraska–Lincoln, Summer 8 2015. http://digitalcommons.unl.edu/chemistrydiss/61

[23] Berutti FA, Alves AK, Bergmann CP, Clemens FJ, Graule T. Synthesis of CeO_2 and Y_2O_3-doped CeO_2 composite fibers by electrospinning. Particulate Science and Technology. 2009;**27**:203-209. DOI: 10.1080/02726350902921681

[24] Li M, Ren W, Wu R, Zhang M. CeO_2 enhanced ethanol sensing performance in a CdS gas sensor. Sensors. 2017;**17**:1577. DOI: 10.3390/s17071577

[25] Gotte A, Spångberg D, Hermansson K, Baudin M. Molecular dynamics study of oxygen self-diffusion in reduced CeO_2. Solid State Ionics. 2007;**178**:1421-1427. DOI: 10.1016/j.ssi.2007.08.003

[26] Zhao S, Gorte RJ. The effect of oxide dopants in ceria on n-butane oxidation. In: Department of Chemical & Biomolecular Engineering Departmental Papers (CBE). University of

Pennsylvania; 2003. Published in Applied Catalysis A: General. 8 August 2003;**248**(1-2): 9-18. Publisher URL: http://dx.doi.org/10.1016/S0926-860X(03)00102-9

[27] Durrani SMA, Al-Kuhaili MF, Bakhtiari IA, Haider MB. Investigation of the carbon monoxide gas sensing characteristics of tin oxide mixed cerium oxide thin films. Sensors. 2012; **12**:2598-2609. DOI: 10.3390/s120302598

[28] Xu Q-H, Xu D-M, Guan M-Y, Guo Y, Qi Q, Li G-D. $ZnO/Al_2O_3/CeO_2$ composite with enhanced gas sensing performance. Sensors and Actuators B. 2013;**177**:1134-1141. DOI: 10.1016/j.snb.2012.12.029

[29] Neri G, Bonavita A, Rizzo G, Galvagno S, Capone S, Siciliano P. Methanol gas-sensing properties of CeO_2–Fe_2O_3 thin films. Sensors and Actuators B. 2006;**114**:687-695. DOI: 10.1016/j.snb.2005.06.062

[30] Pandeeswari R, Jeyaprakash BG. CeO_2 thin film as a low-temperature formaldehyde sensor in mixed vapour environment. Bulletin of Materials Science. October 2014;**37**(6): 1293-1299. DOI: 10.1007/s12034-014-0074-6

[31] Pedhekar RB, Raghuwanshi FC. CeO_2 activated ZnO-TiO_2 thick film for CO_2 gas sensor. International Journal of Engineering Science Invention. 2017;**6**(8):20-28. www.ijesi.org

[32] Abdollahzadeh Ghom S, Andreu T, Zamani C, Morante JR. Mesoporous ceria-zirconia solid solutions as oxygen gas sensing material using high temperature hot plates. In: Proceedings Conference: Semiconductor Conference (CAS), Sinaia, Romania, October 15-17, 2012. 2012;**2**:277-280. DOI: 10.1109/SMICND.2012.6400786

[33] Analog Devices, 30 V, high speed, low noise, low bias current. JFET Operational Amplifier ADA4627-1/ADA4637-1, Data Sheet; 2012

[34] Sheingold D, editor. Transducer Interfacing Handbook. Analog Devices, Incorporated; 1980. Norwood, Massachusetts, U.S.A: Published by Analog Devices, Inc. ISBN 0-916550

[35] de Oliveira Jardim E, Rico-Francés S, Abdelouahab-Reddam Z, Coloma F, Silvestre-Albero J, Sepúlveda-Escribano A, et al. High performance of Cu/CeO_2-Nb_2O_5 catalysts for preferential CO oxidation and total combustion of toluene. Applied Catalysis A: General. 2015;**502**:129-137. DOI: 10.1016/j.apcata.2015.05.033

[36] Norby T. A Kröger-Vink compatible notation for defects in inherently defective sublattices. Journal of the Korean Ceramic Society. 2010;**47**(1):19-25. DOI: 10.4191/KCERS.2010.47.1.019

[37] Leung E. Mechanistic investigation of novel niobium-based materials as enhanced oxygen storage components and innovative CO oxidation catalyst support for environmental emission control systems [PhD thesis]. Columbia University: Columbia/Academic Commons; 2016. https://doi.org/10.7916/D8N016FM

[38] Raba AM, Bautista-Ruíz J, Joya MR. Synthesis and structural properties of niobium pentoxide powders: A comparative study of the growth process. Materials Research. 2016; **19**(6):1381-1387. DOI: 10.1590/1980-5373-MR-2015-0733

[39] Pîslaru-Dănescu L, Telipan G. Sensing element for CO_2 detector based on CeO_2-Nb_2O_5 mixed semiconductor oxides with interfacing electronic circuit for signal conditioning. In: Proceedings IEEE Sensor Applications, SAS. IEEE; February 23–25, 2010, Limerick, Ireland. Catalog Number: ISBN: CFP10SAS-PRT

[40] Yen-Pei F. Ionic conductivity and mechanical properties of Y_2O_3-doped CeO_2 ceramics synthesis by microwave-induced combustion. Ceramics International. 2009;**35**:653-659. DOI: 10.1016/j.ceramint.2008.01.027

[41] Yamashita K, Ramanujachary KV, Greenblatt M. Hydrothermal synthesis and low temperature conduction properties of substituted ceria ceramics. Solid State Ionics. 1995;**81**(1-2): 53-60. DOI: 10.1016/0167-2738(95)99031-H

[42] Goto Y, Takahashi K, Omata T, Otsuka-YaoMatsuo S. Synthesis of Y_2O_3-doped CeO_2 nanocrystals and their surface modification. Journal of Physics: Conference Series. 2009; **165**:012041. DOI: 10.1088/1742-6596/165/1/012041

[43] Yue HM, Liu ZL, Wang Y, Yao KL. Electrical properties of nanocrystalline CeO_2–Y_2O_3 thin films prepared by the sol-gel method. Inorganic Materials. 2003;**39**(7):720-772. DOI: 0020-1685/03/3907

[44] Gabriela T, Lucian P-D, Virgil M, Ionela PP, Dragos O. Preparation and characterization of CeO_2–Y_2O_3 binary-oxides and their CO_2 gas-sensing properties. Sensor Letters. February 2016;**14**(2):114-121(8). DOI: 10.1166/sl.2016.3604

[45] Hummers William S, Offeman RE. Preparation of graphitic oxide. Journal of the American Chemical Society. March 1958;**80**(6):1339. DOI: 10.1021/ja01539a017

[46] Mogaldea G, Ion I, Sandu O, Stamatin I, Dumitru BA, Mogaldea M. Structural investigation of the graphite oxide and thermal reduced graphite oxide with terahertz spectroscopy. Optoelectronics and Advanced Materials–Rapid Communications. September 2011; **5**(9):973-976

[47] Ansari SA, Khan MM, Ansari MO, Kalathil S, Leea J, Cho MH. Band gap engineering of CeO_2 nan ostructure using an electrochemically active biofilm for visible light applications. RSC Advances. 2014;**4**:16782-16791. DOI: 10.1039/c4ra00861h

[48] Talam S, Karumuri SR, Gunnam N. Synthesis, characterization, and spectroscopic properties of ZnO nanoparticles. International Scholarly Research Network ISRN Nanotechnology. 2012;**6**(372505):1-6. DOI: 10.5402/2012/372505

[49] Goharshadi EK, Samiee S, Nancarrow P. Fabrication of cerium oxide nanoparticles: Characterization and optical properties. Journal of Colloid and Interface Science. 2011;**356**: 473-480. DOI: 10.1016/j.jcis.2011.01.063

[50] Tan LL, Ong WJ, Chai SP, Mohamed AR. Reduced graphene oxide-TiO_2 nanocomposite as a promising visible-light-active photocatalyst for the conversion of carbon dioxide. Nanoscale Research Letters. 2013;**8**(1):465. DOI: 10.1186/1556-276X-8-465

[51] Tongguang X, Zhang L, Cheng H, Zhu Y. Significantly enhanced photocatalytic performance of ZnO via graphene hybridization and the mechanism study. Applied Catalysis B: Environmental. January 2011;**101**(3-4):382-387. DOI: 10.1016/j.apcatb.2010.10.007

[52] Wu Chen TS, Weng SC, Lin CN, Lai CH, Huang YJ, Jeng HT, et al. Dramatic band gap reduction incurred by dopant coordination rearrangement in Co-doped nanocrystals of CeO_2. Scientific Reports. 2017;**7**:4715. DOI: 10.1038/s41598-017-05046-0

[53] Ruiz-Trejo E. The optical band gap of Gd-doped CeO_2 thin films as function of temperature and composition. Journal of Physics and Chemistry of Solids. 2013;**74**(4):605-610. DOI: 10.1016/j.jpcs.2012.12.014

[54] Tsang C, Bulpitt C. Rare earth oxide sensors for ethanol analysis. Sensors and Actuators B. 1998;**52**(3):226-235. DOI: 10.1016/S0925-4005(98)00233-0

[55] El-Sayed AM, Ismail FM, Khder MH, Yakout SM. Effect of ceo_2 doping on the structure, electrical conductivity and ethanol gas sensing properties of nanocrystalline zno sensors. International Journal on Smart Sensing and Intelligent Systems. September 2012;**5**(3). DOI: 10.21307/ijssis-2017-498

[56] Yakout SM. Highly sensing properties sensors based on CeDoped ZnO and SnO_2 nanoparticles to ethanol gas. IBIMA Publishing Journal of Research in Nanotechnology. 2016; **2016**:14. http://www.ibimapublishing.com/journals/NANO/nano.html Article ID 690025. DOI: 10.5171/2016.690025

[57] Lungu MV, Vasile E, Lucaci M, Pătroi D, Mihăilescu N, Grigore F, et al. Investigation of optical, structural, morphological and antimicrobial properties of carboxymethyl cellulose capped Ag-ZnO nanocomposites prepared by chemical and mechanical methods. Materials Characterization, ISSN 1044-5803. October 2016;**120**:69-81. DOI: 10.1016/j.matchar.2016.08.022

[58] Lungu M, Gavriliu S, Enescu E, Ion I, Bratulescu A, Marutescu GML, et al. Silver–titanium dioxide nanocomposites as effectiveantimicrobial and antibiofilm agents. Journal of Nanoparticle Research. 2014;**16**:2203. DOI: 10.1007/s11051-013-2203-3

[59] Li B, Liu T, Wang Y, Wang Z. ZnO/graphene-oxide nanocomposite with remarkably enhanced visible-light-driven photocatalytic performance. Journal of Colloid and Interface Science. 2012;**377**:114-121. DOI: 10.1016/j.jcis.2012.03.060

[60] Debanath MK, Karmakar S. Study of blue shift of optical band gap in zinc oxide (ZnO) nanoparticles prepared by low-temperature wet chemical method. Materials Letters. 2013; **111**:116-119. DOI: 10.1016/j.matlet.2013.08.069

[61] Liewhiran C, Phanichphant S. Effects of palladium loading on the response of a thick film flame-made ZnO gas sensor for detection of ethanol vapor. Sensors. 2007;**7**(7):1159-1184. DOI: 10.3390/s7071159

[62] Hongsith N, Choopun S. Effect of platinum impregnation on ZnO tetrapods for ethanol sensor. Advanced Materials Research. 2008;**55**(57):289-292. DOI: 10.4028/www.scientific.net/AMR.55-57.289

[63] Wongrat E, Pimpang P, Choopun S. Comparative study of ethanol sensor based on gold nanoparticles: ZnO nanostructure and gold: ZnO nanostructure. Applied Surface Science. 2009;**256**(4):968-971. DOI: 10.1016/j.apsusc.2009.02.046

[64] Paraguay FD, Miki-Yoshida M, Morales J, Solis J, Estrada WL. Influence of Al, In, Cu, Fe and Sn dopants on the response of thin film ZnO gas sensor to ethanol vapour. Thin Solid Films. 2000;**373**(1-2):137-140. DOI: 10.1016/S0040-6090(00)01120-2

[65] Zheng K, Gu L, Sun D, Mo X, Chen G. The properties of ethanol gas sensor based on Ti doped ZnO nanotetrapods. Materials Science and Engineering B. 2010;**166**(1):104-107. DOI: 10.1016/j.mseb.2009.09.029

[66] Peng L, Xie T-F, Yang M, Wang P, Xu D, Pang S, et al. Light induced enhancing gas sensitivity of copper-doped zinc oxide at room temperature. Sensors and Actuators B. 2008;**131**(2):660-664. DOI: 10.1016/j.snb.2007.12.060

[67] Li Y-J, Li K-M, Wang C-Y, Kuo C-I, Chen L-J. Low-temperature electrodeposited Co-doped ZnO nanorods with enhanced ethanol and CO sensing properties. Sensors and Actuators B. 2012;**161**(1):734-739. DOI: 10.1016/j.snb.2011.11.024

[68] Navale SC, Ravi V, Mulla IS. Investigations on Ru doped ZnO: Strain calculations and gas sensing study. Sensors and Actuators B. 2009;**139**(2):466-470. DOI: 10.1016/j.snb.2009.03.068

[69] Mohandoss M, Gupta SS, Nelleri A, Pradeep T, Maliyekkal SM. Solar mediated reduction of graphene oxide. RSC Advances. 2017;**7**:957-963. DOI: 10.1039/C6RA24696F

[70] Afzal NC, Sabbatini L, Torsi L. NOx sensors based on semiconducting metal oxide nanostructures. Progress and perspectives. Sensors and Actuators B. Chemical. 2012; **171-172**:25-42. DOI: 10.1016/j.snb.2012.05.026

[71] Zhang L, Fang Q, Huang Y, Xu K, Ma F, Chu PK. Facet-engineered CeO_2/graphene composites for enhanced NO_2 gas-sensing. Journal of Materials Chemistry C. 2017;**5**: 6973-6981. DOI: 10.1039/C7TC01523B

[72] Zhao F, Zhao Y, Chen N, Qu L. Stimuli-deformable graphene materials: From nanosheet to macroscopic assembly. Materials Today. 2016;**19**(3):146-156, http://creativecommons.org/licenses/by-nc-nd/4.0/. DOI: 10.1016/

[73] Chammingkwan P, Matsushita K, Taniike T, Terano M. Enhancement in mechanical and electrical properties of polypropylene using graphene oxide grafted with end-functionalized polypropylene. Materials. 2016;**9**:240. DOI: 10.3390/ma9040240

[74] Zumbahlen H, editor. Basic Linear Design. Analog Devices, Incorporated; 2007. Norwood, Massachusetts, U.S.A: Published by Analog Devices, Inc. ISBN 0-916550-28-1

[75] Sheingold D, editor. Multiplier Application Guide. Analog Devices, Incorporated; 1978. Norwood, Massachusetts, U.S.A: Published by Analog Devices, Inc.

[76] Kester W, editor. Practical Design Techniques for Sensor Signal Conditioning. Analog Devices; 1999. Norwood, Massachusetts,U.S.A: Published by Analog Devices, Inc. ISBN-0-916550-20-6

[77] Sheingold D. Nonlinear Circuits Handbook. Analog Devices; 1976. Norwood, Massachusetts, U.S.A: Published by Analog Devices, Inc